Precise measurement of Bhabha scattering at a center-of-mass energy of 57.77 GeV

T. Arima,[3,*] S. Odaka,[2,†] K. Ogawa,[2,‡] J. Shirai,[2] T. Tsuboyama,[2] N. Hosoda,[4,§] M. Miura,[3,‖] K. Abe,[1] K. Amako,[2] Y. Arai,[2] Y. Asano,[3] M. Chiba,[4] Y. Chiba,[5] M. Daigo,[6] M. Fukawa,[2,¶] Y. Fukushima,[2] J. Haba,[1,**] H. Hamasaki,[3] H. Hanai,[7] Y. Hemmi,[8] M. Higuchi,[9] T. Hirose,[4] Y. Homma,[10] N. Ishihara,[2] Y. Iwata,[11] J. Kanzaki,[2] R. Kikuchi,[8] T. Kondo,[2] T. T. Korhonen,[2,12,††] H. Kurashige,[8] E. K. Matsuda,[13] T. Matsui,[2] K. Mikaye,[8] S. Mori,[3] Y. Nagashima,[7] Y. Nakagawa,[14] T. Nakamura,[15] I. Nakano,[16,‡‡] T. Ohama,[2] T. Ohsugi,[11] H. Ohyama,[17] K. Okabe,[13] A. Okamoto,[8] A. Ono,[18] J. Pennanen,[2,12] H. Sakamoto,[8] M. Sakuda,[2] M. Sato,[9] N. Sato,[2] M. Shioden,[19] T. Sumiyoshi,[2] Y. Takada,[3] F. Takasaki,[2] M. Takita,[7] N. Tamura,[13,§§] D. Tatsumi,[7] K. Tobimatsu,[20] S. Uehara,[2] Y. Unno,[2] T. Watanabe,[21] Y. Watase,[2] F. Yabuki,[4] Y. Yamada,[2] T. Yamagata,[14] Y. Yonezawa,[22] H. Yoshida,[23] and K. Yusa[3]

(VENUS Collaboration)

[1]*Department of Physics, Tohoku University, Sendai 980, Japan*
[2]*KEK, National Laboratory for High Energy Physics, Tsukuba 305, Japan*
[3]*Institute of Applied Physics, University of Tsukuba, Tsukuba 305, Japan*
[4]*Department of Physics, Tokyo Metropolitan University, Hachioji 192-03, Japan*
[5]*Yasuda Women's Junior College, Hiroshima 731-01, Japan*
[6]*Faculty of Economics, Toyama University, Toyama 930, Japan*
[7]*Department of Physics, Osaka University, Toyonaka 560, Japan*
[8]*Department of Physics, Kyoto University, Kyoto 606, Japan*
[9]*Department of Applied Physics, Tohoku-Gakuin University, Tagajo 985, Japan*
[10]*Faculty of Engineering, Kobe University, Kobe 657, Japan*
[11]*Department of Physics, Hiroshima University, Higashi-Hiroshima 724, Japan*
[12]*Research Institute for High Energy Physics, Helsinki University, SF-00170 Helsinki, Finland*
[13]*Department of Physics, Okayama University, Okayama 700, Japan*
[14]*International Christian University, Mitaka 181, Japan*
[15]*Faculty of Engineering, Miyazaki University, Miyazaki 889-01, Japan*
[16]*Institute of Physics, University of Tsukuba, Tsukuba 305, Japan*
[17]*Hiroshima National College of Maritime Technology, Higashino 725-02, Japan*
[18]*Faculty of Cross-Cultural Studies, Kobe University, Kobe 657, Japan*
[19]*Ibaraki College of Technology, Katsuta 312, Japan*
[20]*Center for Information Science, Kogakuin University, Tokyo 163-91, Japan*
[21]*Department of Physics, Kogakuin University, Hachioji 192, Japan*
[22]*Tsukuba College of Technology, Tsukuba 305, Japan*
[23]*Naruto University of Education, Naruto 772, Japan*

(Received 17 June 1996)

Bhabha scattering at a center-of-mass energy of 57.77 GeV has been measured using the VENUS detector at KEK TRISTAN. The precision is better than 1% in scattering angle regions of $|\cos\theta| \leqslant 0.743$ and $0.822 \leqslant \cos\theta \leqslant 0.968$. A model-independent scattering-angle distribution is extracted from the measurement. The distribution is in good agreement with the prediction of the standard electroweak theory. The sensitivity to underlying theories is examined, after unfolding the photon-radiation effect. The q^2 dependence of the photon vacuum polarization, frequently interpreted as a running of the QED fine-structure constant, is directly observed with a significance of three standard deviations. The Z^0 exchange effect is clearly seen when the distribution is compared with the prediction from QED (photon exchanges only). The agreement with the standard theory leads us to constraints on extensions of the standard theory. In all quantitative discussions, correlations in the systematic error between angular bins are taken into account by employing an error matrix technique. [S0556-2821(97)00801-1]

PACS number(s): 13.10.+q, 12.60.Cn, 14.60.Cd, 14.80.−j

*Present address: Faculty of Engineering, Kyushu University, Fukuoka 812, Japan.
†Corresponding author. Electronic address: odaka@kekvax.kek.jp.
‡Deceased.
§Present address: Japan Synchrotron Radiation Research Institute, Kamigouri 678-12, Japan.
‖Present address: Institute for Cosmic Ray Research, University of Tokyo, Tanashi 188, Japan.
¶Present address: Naruto University of Education, Naruto 772, Japan.
**Present address: KEK, Tsukuba 305, Japan.
††Present addresss: Accelerator Division, KEK, Tsukuba 305, Japan.
‡‡Present address: Department of Physics, Okayama University, Okayama 700, Japan.
§§Present address: Department of Physics, Niigata Umiversity, Niigata 950-21, Japan.

I. INTRODUCTION

Bhabha scattering, $e^+e^- \to e^+e^-$, is the most fundamental reaction in e^+e^- collisions. The reaction at high energies has been extensively studied by experiments at e^+e^- colliders [1–4]. Apart from the intrinsic interest concerning the underlying physics, the study is important since the luminosity of the e^+e^- collisions is usually determined by using this reaction.

In the framework of the standard electroweak theory [5], Bhabha scattering is described by t-channel (spacelike) and s-channel (timelike) exchanges of the photon and the Z^0 boson between the electrons. The validity of this picture has been precisely demonstrated at collision energies far below the Z^0 resonance [3] and on the resonance [4]. In the former the reaction is dominated by the photon exchange. The contribution of the Z^0 exchange has been marginal in the observations. On the other hand, the Z^0 contribution is obvious on the resonance. The validity of theoretical predictions concerning the coupling between Z^0 and the electron has been precisely examined. However, since the direct production of Z^0 dominates the contribution there, the measurements are relatively insensitive to the interferences between the Z^0 and photon exchanges.

Therefore, in order to complete the verification, it is necessary to carry out high-precision measurements at intermediate energies where the interferences are expected to become appreciable. In addition, such measurements are expected to have good sensitivity to unexpected new interactions, to which experiments on the resonance are blinded by the large contribution from the resonance.

In this work, we present results from a measurement of Bhabha scattering, carried out using the VENUS detector at the TRISTAN e^+e^- collider at KEK. The measurement is based on high-statistics data at a center-of-mass (c.m.) energy of 57.77 GeV, corresponding to an integrated luminosity of about 290 pb^{-1}, accumulated from 1991 until the end of the experiment in May 1995. The measurement has been carried out with a precision of 0.5% in a central (barrel) region, $|\cos\theta| \leqslant 0.743$, and 0.7% in a forward (end-cap) region, $0.822 \leqslant \cos\theta \leqslant 0.968$.

In our previous report [1] and all other reports from experiments below the Z^0 resonance [2,3], the measurements were presented in the form of a tree-level cross section. A correction for radiative effects is indispensable in such analyses. The method relied on theoretical calculations of the first-order QED [6] or electroweak [7,8] corrections. On the other hand, the real phenomena include radiative effects up to infinite order, allowing an arbitrary number of photon emissions. We are now aware that the second-order QED correction amounts to a level of 1% of the tree-level cross section [9,10] so that the previous experimental results may be incorrect at this level. Note that still-missing higher orders may alter the correction at a similar level.

In order to be free from such ambiguities irrelevant to the experimental reliability, we present our primary result, a scattering angle distribution, in a model-independent way. The result is dependent on the experimental conditions. However, since the condition is well defined, the result can be compared with theoretical predictions, at least the prediction from the standard electroweak theory, by using computer programs [9,10].

In order to proceed to further discussions, the model-independent result is converted to a form which is independent of experimental conditions, being based on certain theoretical estimations of the radiative correction. If theoretical improvements are made in the future, the discussions can be revised without any ambiguity by starting from the primary model-independent result.

A reliable estimation of systematic errors is crucial in high-precision measurements. Corrections for the detection inefficiency and the background contamination frequently give systematic errors having a certain correlation between the measurements. In the present analysis, error correlations between angular bins are treated in the form of an error (covariance) matrix. The correlation matrix, the nondimensional component of the error matrix, is explicitly presented as a result of the measurement.

The layout of this work is as follows. The experimental apparatus is described in Sec. II. Relevant features of the TRISTAN storage ring are briefly summarized, along with a detailed description about the VENUS detector and event triggers. Event analyses in the barrel region and in the end-cap region are described in Secs. III and IV, separately. Corrections and associated systematic errors are described in detail. Section V is dedicated to discussions of underlying physics. The obtained experimental result is compared with the prediction from the standard theory; then, possibilities of its extension and new physics are discussed. Finally, the conclusions are summarized in Sec. VI.

II. EXPERIMENTAL APPARATUS

A. TRISTAN MR

The TRISTAN main ring (MR) was an e^+e^- storage ring of about 3 km in circumference [11]. It was operated with four beam bunches, two electron bunches, and two positron bunches circulating in opposite directions. Collisions occurred every 5 μs, at four interaction points on the ring. A typical beam current was about 15 mA at the start of the collisions and fell thereafter with a typical lifetime of 200 min.

During an upgrade in 1990, a pair of superconducting quadrupole magnets were installed at the four interaction regions. The vertical beam size at the interaction points was squeezed to one-half of the previous value, and a maximum luminosity of 4×10^{31} $\mathrm{cm}^{-2}\,\mathrm{s}^{-1}$ was achieved. After the upgrade, the collision energy was fixed mostly at 58 GeV to provide the experiments with high-statistics collision data, until the end of the operation in May 1995.

The beam energy of MR was measured by means of resonant spin depolarization [12]. Under a typical operation condition, the actual beam energy was smaller than the nominal value by 114 MeV for the nominal beam energy of 29.0 GeV [13], i.e., the actual c.m. energy ($\sqrt{s}$) was 57.77 GeV for the nominal c.m. energy of 58.0 GeV. The uncertainty was estimated to be a few MeV from the possible instability and uncertainties in the accelerator components [14]. The spread of the beam energy was 48 MeV in rms, resulting in a c.m. energy spread of 68 MeV [13].

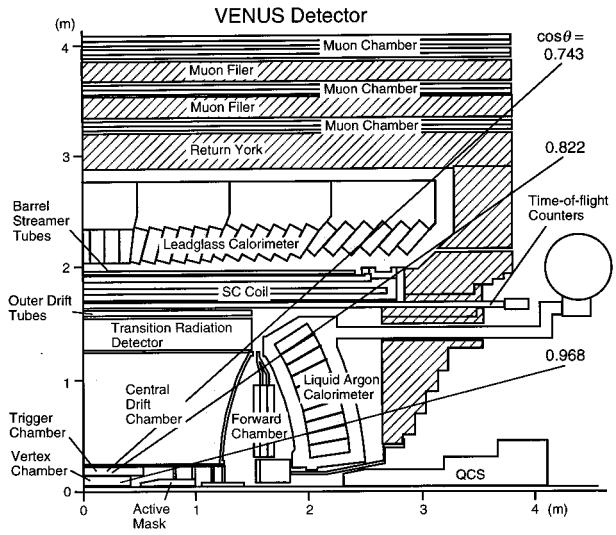

FIG. 1. Quadrant cross section of the VENUS detector after the upgrade. The edges of the angular acceptance are indicated.

The energy imbalance between the electron beams and the positron beams may have been sizable, since the energy loss of beam particles during the circulation was large. Such an imbalance will cause a mismatch in the scattering angles of two back-to-back particles. A significant mismatch was observed in Bhabha scattering events in the 1987 runs. The mismatch corresponded to an imbalance, $[E(e^-)-E(e^+)]/[E(e^-)+E(e^+)]$, at a level of 0.2%. Thanks to a careful operation of the accelerator, the imbalance was eliminated to an invisible level, $<0.05\%$, in data relevant to the present analysis.

B. Overview of the VENUS detector

The VENUS detector was a general-purpose magnetic spectrometer, covering almost the full solid angle around one of the four interaction points of TRISTAN MR. The detector was upgraded in 1990, at the same time as the accelerator upgrade. The detector before the upgrade is described elsewhere [15]. In the upgrade, the beam pipe was reduced in radius from 10 to 5 cm, and an inner chamber, formerly used for an event trigger, was replaced with a vertex chamber [16] and a new trigger chamber. Furthermore, a large transition radiation detector [17] was installed in order to improve the capability of electron identification. A quadrant cross section of the upgraded VENUS detector is shown in Fig. 1.

Tracking devices placed inside a 7.5 kG axial magnetic field, produced by a solenoidal superconducting magnet coil [18], were the vertex chamber, the trigger chamber, the central drift chamber (CDC) [19] and the outer drift tubes (ODT), from inside to outside. The transition radiation detector was placed between CDC and ODT. Time-of-flight counters (TOF) [20] were placed inside of the magnet coil, providing time-of-flight and trigger information. The forward chambers were placed so as to enhance the tracking capability in a small-angle region.

Calorimeters covered almost the full solid angle without any apparent gaps, down to 40 mrad of the angle (θ) from the beam axis. A lead glass array (LG) [21] placed outside of the magnet coil covered a central (barrel) region, $|\cos\theta|\leq 0.8$. Forward (end-cap) regions, $0.79\leq|\cos\theta|\leq 0.99$, were covered with a pair of lead-liquid argon sandwich calorimeters (LA) [22]. Further small angles were covered with a pair of active masks (AM) [23], composed of lead cylinders interleaved with scintillation fibers.

Plastic streamer tubes (BST) were placed in front of the lead glass array in order to provide photon-conversion information. BST had a two-dimensional tracking capability utilizing both anode and cathode readouts. The muon chambers [24] were placed outside of the iron return yoke in order to identify high-momentum muons. The chambers were divided into four superlayers interleaved with iron filters.

The detector was so placed that the collisions should occur near its center. The observed offset of the average collision point was 5 mm and 0.3 mm along and transverse to the beam direction, respectively. The movement of the average position was within ± 1 mm in both directions throughout the data-taking period. The spread of the interaction point along the beam direction was measured to be a Gaussian distribution with a standard deviation of 1.0 cm. The present measurement is insensitive to the transverse spreads of 300 μm horizontally and 20 μm vertically.

Detector components relevant to the present analysis are CDC, LG, and LA. Relevant features of these devices and event triggers are described in the following subsections.

C. Central drift chamber

The central drift chamber (CDC) [19] was the main charged-particle tracking device of the VENUS detector. It was a conventional cylindrical multiwire drift chamber with a length of 3 m. The inner and outer radii of the gas volume were 25 and 126 cm, respectively. The chamber was filled with a gas mixture of an Ar/CO_2/methane (89/10/1), so-called HRS gas, at atmospheric pressure.

The chamber consisted of 7104 almost identical single-hit drift cells of 1.7 cm in the radial direction and typically 2 cm in full width. The cells were arranged in 29 cylindrical layers, coaxially surrounding the center axis of the chamber. The innermost layer was at 28.65 cm in radius, and the outermost one was at 121.35 cm. The layers were grouped to form 10 superlayers. Each superlayer consisted of a pair of axial layers staggered by a half cell and one small angle (about 3°) stereo layer, except for the innermost superlayer. Charged particles emitted in the central region, $|\cos\theta|\leq 0.75$, penetrated the sensitive region of all layers.

The momentum resolution of CDC in the 7.5 kG magnetic field was measured to be

$$\frac{\sigma_p}{p}=\sqrt{(0.013)^2+[0.008\times p_t(\mathrm{GeV}/c)]^2} \qquad (1)$$

in the central region, where p_t is the transverse momentum measured with respect to the beam axis. The polar angle (θ) resolution was measured from the consistency between the scattered angles of two electrons in Bhabha events. Comparing the result with a simulation, as shown in Fig. 2, the resolution was found to be

$$\sigma(\cot\theta)=(0.8\pm 0.1)\times 10^{-2}. \qquad (2)$$

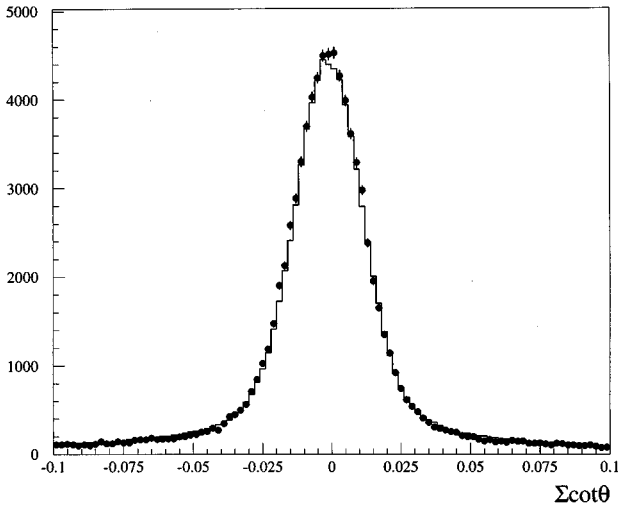

FIG. 2. Sum of $\cot\theta$ of the two electrons in Bhabha-scattering events, measured by CDC. The spread of the distribution represents the polar angle (θ) resolution of CDC. The measurement (plot) is compared with the result from a simulation (histogram) where the nominal value of the resolution is assumed. The long tails are an effect of the photon radiation.

The detection efficiency was better than 99.5% per sampling on the average, including the inefficiency due to dead channels. We found 12 dead channels in total, including 4 channels in which the sense wires were known to be defective. The tracking capability was insensitive to this amount of small inefficiency.

D. Lead glass calorimeter

The lead glass calorimeter array (LG) [21] consisted of 5160 lead glass counters of approximately 12×12 cm^2 in cross section and 30 cm in length. The length corresponded to 18 radiation lengths. The counters were arranged in a cylindrical array surrounding the beam line, 120 counters in the azimuth and 43 counters along the beam line, covering polar angles (θ) from 37° to 143°. All of the counters were approximately pointing towards the interaction point with small tilts in both directions (semitower geometry).

The intrinsic energy resolution, measured by using electron beams prior to the installation, was $\sigma_E/E=1.0\%+3.0\%/\sqrt{E(\mathrm{GeV})}$ for counters in a central region, $42°\leqslant\theta\leqslant138°$ and $\sigma_E/E=1.25\%+5.0\%/\sqrt{E(\mathrm{GeV})}$ for other counters, because different types of photomultipliers were used. The resolution of the injection point, measured from energy sharing between counters, was 1.2 cm on the average.

The resolutions were deteriorated by materials at smaller radii at low energies, and by calibration errors at high energies. The dominant material placed in front of the LG was the solenoid magnet with a radial thickness of 0.5 radiation length. The average resolution was degraded to 7% for 1.5 GeV electrons from the two-photon process. The gain of the counters had been calibrated using electron beams prior to the installation, and tracked during the experiment by using a monitor system employing xenon flash tubes and optical fibers. After a correction based on the monitor results, the average resolution was 3.8% for 30 GeV electrons from Bhabha scattering.

E. Liquid-argon calorimeter

The liquid-argon calorimeter (LA) [22] consisted of two independent lead-liquid argon sandwich counters. The counters were placed at about 2 m from the interaction point, covering polar angles from 8° to 37°. Each counter consisted of 480 tower-structure radiator modules, a stack of 71 lead plates of 1.5 mm in thickness with a plate gap of 3 mm. The radiator plates served as electrodes. The modules were enclosed in a Dewar filled with liquid argon. The total thickness of the calorimeter corresponded to 20.3 radiation lengths, including the liquid argon.

The modules were arranged in 10 concentric columns (rings). One module had a polar-angle coverage of 2.9°. The gap between the modules was 2 mm. In order to reduce module-gap effects, the modules were arranged in a semitower geometry, pointing towards 79 cm beyond the interaction point. Further, in the signal readout, each module was longitudinally subdivided into four segments of an approximately equal thickness.

The intrinsic energy resolution of LA was about $\sigma_E/E=10\%/\sqrt{E(\mathrm{GeV})}$. The resolution of the injection point, measured from energy sharing between the modules, was 6 mm on the average. The resolutions were degraded by materials placed in front of the calorimeter, such as the endplates and electronics components of CDC. The materials of the vertex chamber, the trigger chamber, and their readout electronics affected the resolution at small angles significantly. Their effects were carefully investigated in the course of the analysis. The calibration error was smaller than 1% because the amplifiers had been carefully calibrated prior to the installation [22].

F. Event trigger

The data acquisition was triggered by the coincidence between beam-crossing signals and signals issued by trigger-generation circuits. The inputs of the trigger-generation circuits were analog-sum signals from calorimeters and track patterns reconstructed from CDC and TOF hits.

The analog signals from LG were added in every digitizer module to provide segment-sum signals. The segment typically corresponded to a 6×15 array of the LG modules. We had 58 segments in total, 8 or 10 segments in azimuth and 7 segments along the beam direction. The segment-sum signals were further added to provide a total-sum signal.

LA was subdivided into 24 segments in each counter, 12 sectors in azimuth and 2 segments by the polar angle. Each segment provided an analog segment-sum signal. The signals were further added to provide a total-sum signal in each counter. AM was subdivided into four sectors in each side.

The axial-layer cells of CDC were grouped to form 64 trigger-cells in each superlayer, divided in azimuth. Track-finder modules recognized tracks by comparing the trigger-cell hit pattern from inner seven superlayers with a preloaded lookup table [25]. The pattern of the lookup table was so defined that the track finders should have nearly full efficiency for high transverse momentum ($p_t\geqslant1$ GeV/c) tracks.

The trigger-generation circuits issued a trigger signal when at least one of the following conditions was satisfied: (i) The pulse height of the LG total-sum signal exceeded a threshold corresponding to an energy deposit of 3 GeV; (ii) a pair of coplanar ($\phi_{\rm acop}\leqslant 10°$) tracks were recognized by the track finder and TOF hits were found in a reasonable range around the tracks, where $\phi_{\rm acop}$ is the supplement of the opening angle in the projection onto the plane perpendicular to the beam direction; (iii) a pair of coplanar ($\phi_{\rm acop}\leqslant 30°$) tracks were recognized by the track finder and TOF hits were found in a reasonable range around the tracks; (iv) two or more tracks were recognized by the track finder, and the pulse height of at least one LG segment-sum signal exceeded a threshold of 0.7 GeV; (v) the pulse height of at least one of the two LA total-sum signals exceeded a threshold of 4 GeV; (vi) at least one back-to-back pair of AM segments had energy deposits consistent with Bhabha scattering events.

Condition (ii) was totally contained in condition (iii). The former was kept for a crosscheck because the generation circuits were independent of each other. A trigger-generation circuit using the LA segment-sum signals was turned off throughout the relevant period, in order to avoid a high trigger rate. Trigger (vi) was mainly used for an on-line luminosity monitor. Additionally, trigger signals were generated at a frequency of 0.1 Hz, regardless of the detector signals. These data provided bias-free information concerning the data quality.

When the data acquisition was triggered, digitized data were collected by a FASTBUS processor module prior to the transfer to an on-line computer. Utilizing the data collection time, a software selection was applied in the processor module to those events which were triggered by condition (iii) alone [26]. Tighter association between CDC tracks and TOF hits was required in order to reduce events from beam-beam pipe interactions.

III. ANALYSIS IN THE BARREL REGION

A. Event selection

The signature of Bhabha scattering events is an observation of a pair of back-to-back (collinear) electron and positron, each having the beam energy ($E_{\rm beam}$). Such electrons leave large deposits in electromagnetic calorimeters. The signature is diluted by radiative effects, resulting in extra photon emissions, and electromagnetic interactions of the scattered electrons in detector materials. Besides, detectors have finite resolutions. The selection criteria have to be appropriately relaxed, so as to minimize ambiguities in the detection efficiency.

In the barrel region, we selected candidate events according to the following criteria

(1) Events must comprise 2, 3, or 4 CDC tracks which fulfilled the conditions that (t1) $N_{\rm hit}({\rm axial})\geqslant 8$, (t2) $N_{\rm hit}({\rm stereo})\geqslant 4$, (t3) $|R_{\rm min}|\leqslant 2.0$ cm, (t4) $|Z_{\rm min}|\leqslant 20$ cm, and (t5) $p_t\geqslant 1.0$ GeV/c. $N_{\rm hit}$(axial) and $N_{\rm hit}$(stereo) are the number of axial-wire and stereo-wire hits composing the track, respectively. The parameter $R_{\rm min}$ is the closest approach to the center axis of CDO (z axis) and $Z_{\rm min}$ is the z coordinate at the closest approach.

(2) Among these CDC tracks, at least one of the pairs must satisfy the conditions that (p1) both tracks were within a scattering-angle region of $|\cos\theta|\leqslant 0.743$, (p2) for both tracks, a high-energy LG cluster ($E\geqslant E_{\rm beam}/3$) was observed within 10° around the production direction, and (p3) the acollinearity angle ($\theta_{\rm acol}$), the supplement of the opening angle, was not larger than 10°.

(3) The selected track pair must have opposite charges. When an event included multiple candidate pairs, the pair that had the largest average momentum $\langle p\rangle$, defined as $1/\langle p\rangle=(1/p_1+1/p_2)/2$, was chosen.

The requirements on the track quality, (t1)–(t4), were chosen to be very loose, so as to avoid ambiguities arising from the detailed performance of CDC. Bremsstrahlung in detector materials was widely allowed by loose requirements on the track momentum (t5) and the calorimeter-energy association (p2).

The constraint on the number of tracks, condition (1), allowed for the conversion of an extra photon. The emission of low-energy photons was not restricted, since no constraint was applied to extra calorimeter energies and low-momentum tracks. The angular constraints were determined by the track measurement, (p1) and (p3), while the energy threshold was determined by the calorimeter measurement, (p2). Condition (3) was required in order to uniquely determine the scattering angle. This condition discarded 1.4% of the events.

A total of 96 067 events were selected from 58-GeV data accumulated from 1991 until the end of the experiment in May 1995. The selected sample was subdivided into 12 bins according to the cosine of the scattering angle of the electron. The number of candidate events in each bin (n_i) is listed in Table I.

B. Corrections

1. Definition of the signal

In order to allow comparisons with theoretical predictions, it is necessary to give an explicit definition of the signal that the experiment measures. Such a definition must be easily simulated in theoretical calculations without ambiguity. In addition, it is desired to be as close to the experimental condition as possible, so that we can minimize ambiguities irrelevant to the experiment.

In the barrel region, we define the signal to be those events from the reaction $e^+e^-\rightarrow e^+e^-+n\gamma$ ($n=0,1,\ldots,\infty$), in which the final state consists of a pair of collinear ($\theta_{\rm acol}\leqslant 10°$) e^+ and e^-, both scattered to large angles ($|\cos\theta|\leqslant 0.743$) and carrying a large energy ($E\geqslant E_{\rm beam}/3$). No explicit constraint is imposed on any photon emission. The detection efficiency and background contamination were estimated according to this definition.

2. Detection efficiency

Tracking failure: The tracking efficiency of CDC was estimated using a Bhabha-event sample collected by applying tighter requirements on the LG energies and one of the associated CDC tracks. The quality of the other CDC track was then inspected. The study was carried out by two different methods. In the first, we relied on a good efficiency in the two-dimensional ($x-y$) reconstruction using axial-layer hits, and estimated the failure rate in the z reconstruction. In the second, we required that the two-track trigger (ii) was

TABLE I. Primary results of this experiment. The number of candidates in the barrel region is divided to angular bins (n_i), according to the scattering angle of the electron. Also listed are the number of signal events (N_i) corrected for the detection inefficiency and the background contamination, the angular distribution (R_i) normalized to the signal yield in the end-cap region, and the prediction for R_i from the standard electroweak theory [R_i(EW)] estimated by using ALIBABA. The results from the measurement in the end-cap region are presented at the bottom. The quoted errors are the quadratic sum of the statistical error and the systematic errors. The error correlation is shown in Table IV. The error of R_i does not include the normalization error (0.7%) from the measurement in the end-cap region.

Bin	$\cos\theta$	n_i	N_i (10^3)	R_i (10^{-3})	R_i(EW) (10^{-3})
1	$-0.743\sim-0.619$	1 477	1.472 ± 0.045	1.425 ± 0.044	1.441
2	$-0.619\sim-0.495$	1 623	1.592 ± 0.046	1.542 ± 0.044	1.524
3	$-0.495\sim-0.372$	1 720	1.707 ± 0.047	1.654 ± 0.045	1.618
4	$-0.372\sim-0.248$	1 894	1.887 ± 0.047	1.827 ± 0.046	1.795
5	$-0.248\sim-0.124$	2 163	2.182 ± 0.052	2.113 ± 0.051	2.079
6	$-0.124\sim 0.000$	2 523	2.578 ± 0.054	2.496 ± 0.052	2.540
7	$0.000\sim 0.124$	3 311	3.373 ± 0.065	3.267 ± 0.063	3.282
8	$0.124\sim 0.248$	4 474	4.592 ± 0.077	4.447 ± 0.074	4.516
9	$0.248\sim 0.371$	6 733	6.865 ± 0.091	6.648 ± 0.088	6.658
10	$0.371\sim 0.495$	10 878	11.05 ± 0.12	10.70 ± 0.12	10.76
11	$0.495\sim 0.619$	19 721	20.07 ± 0.17	19.44 ± 0.16	19.42
12	$0.619\sim 0.743$	39 550	40.81 ± 0.26	39.52 ± 0.26	39.65
EC	$0.822\sim 0.968$	1045.1×10^3	1032.6 ± 7.3		

issued. The tracking quality in inefficient events, in which the examined track did not fulfill the requirements in the event selection, was studied visually.

The two methods gave consistent results. The result from the first method is listed in Table II, where the scattering angle was determined by the successfully reconstructed track. The quoted errors are the quadratic sum of the statistical error and a common systematic error of 0.1%, arising from an ambiguity in the event identification. The result corresponds to a total inefficiency of (0.4 ± 0.1)%. From a visual inspection we found that the main reason for the failure was electromagnetic interactions of electrons or associated photons in the detector materials.

Charge misidentification: The signal events were rejected if the charge of either electron was misidentified. The corresponding inefficiency was estimated by using an event sample selected from those events satisfying criteria (1) and (2) in the event selection. A connection of a very large LG energy deposit, more than 90% of the beam energy, was required to one of the CDC tracks, in order to purify the sample. Among these events, 1.2% of the events consisted of a pair of same-charge tracks. The estimated inefficiency, the fraction of the same-charge events, in each angular bin is listed in Table II.

The forward and backward scattering could not be distinguished in this estimation. We assumed that the inefficiency was forward-backward symmetric. Since the events comprise a pair of back-to-back electron and positron, asymmetry could take place only if possible forward-backward asymmetry in the tracking capability of CDC had certain positive-negative charge asymmetry. We found no significant difference between the numbers of positive- and negative-charge events in the same-charge sample. The result on the tracking failure, which is an extreme case of bad quality in the track-

TABLE II. Estimated detection inefficiency in the barrel region.

	Inefficiency (%)					
Bin	Tracking failure	Charge misident.	Brems-strahlung	Angular resolution	Angular accuracy	Dead LG modules
1	0.54 ± 0.23	1.22 ± 1.23	1.46 ± 0.23	0.77 ± 0.29	±0	0.75 ± 0.32
2	0.13 ± 0.14	1.22 ± 1.03	1.06 ± 0.24	0.09 ± 0.30	±0	0.45 ± 0.29
3	0.63 ± 0.22	1.36 ± 0.92	0.93 ± 0.25	-0.10 ± 0.34	±0	0.98 ± 0.46
4	0.41 ± 0.18	1.21 ± 0.63	0.89 ± 0.28	-0.37 ± 0.35	±0	1.33 ± 0.27
5	0.36 ± 0.17	1.20 ± 0.43	0.88 ± 0.30	-0.40 ± 0.34	±0.09	2.28 ± 0.75
6	0.56 ± 0.18	1.40 ± 0.30	1.06 ± 0.34	0.84 ± 0.32	±0.11	1.66 ± 0.34
7	0.52 ± 0.16	1.40 ± 0.26	1.06 ± 0.34	-0.34 ± 0.27	±0.16	1.55 ± 0.63
8	0.57 ± 0.16	1.20 ± 0.25	0.88 ± 0.30	-0.05 ± 0.23	±0.15	2.17 ± 0.64
9	0.68 ± 0.14	1.21 ± 0.23	0.89 ± 0.28	-0.04 ± 0.18	±0.24	1.21 ± 0.24
10	0.34 ± 0.12	1.36 ± 0.20	0.93 ± 0.25	-0.17 ± 0.13	±0.28	0.82 ± 0.22
11	0.37 ± 0.11	1.22 ± 0.15	1.06 ± 0.24	0.16 ± 0.09	±0.33	0.42 ± 0.04
12	0.27 ± 0.10	1.22 ± 0.12	1.46 ± 0.23	1.03 ± 0.14	±0.27	0.59 ± 0.07

ing, indicates that the asymmetry would not be larger than a factor of 2.

Because there was no further evidence supporting the assumption, we assigned such a systematic error to the backward bins that increases in proportion to $|\cos\theta|$ and amounts to 100% of the estimated inefficiency in the most backward bin. Accordingly, the forward bins also suffer from certain systematic errors, since the observed same-charge fraction was an average between the forward and backward bins. In addition, we assigned an overall systematic error of 0.1%, so as to take account of an ambiguity due to small contamination of background events in the used sample. The error quoted in Table II is the quadratic sum of the statistical error and these systematic errors.

Bremsstrahlung: The signal events may have been lost if the momentum loss due to the bremsstrahlung in materials at smaller radii was very large. We estimated the material thickness from the population of low-momentum electron tracks, $p_t \leqslant 1$ GeV/c, in Bhabha scattering events. The event sample was collected by requiring tighter constraints on the LG energies and one of the tracks. The contamination of $e^+e^-\gamma$ events was subtracted statistically. The obtained fraction of low-momentum tracks was compared with the prediction from the formula for bremsstrahlung [27]. The estimation was carried out separately in each angular bin.

A Monte Carlo sample of Bhabha scattering events was used to estimate the inefficiency. The events were generated by the Tobimatsu-Shimizu (TS) program [7], which includes all first-order electroweak corrections. The statistics of the sample was about four times the real data. The momentum loss due to the bremsstrahlung was simulated according to the formula that was used for the estimation of the material thickness. The estimated inefficiency is listed in Table II. The inefficiency is forward-backward symmetric since the events comprise both forward-going and backward-going tracks.

From the above study, the average radial thickness of the materials was estimated to be 11% of a radiation length. On the other hand, counting of known detector materials gave a thickness of 9% of a radiation length. Since the difference may be caused by faults in the estimation method, we assigned an overall systematic error of 15% to the estimated thickness. The errors quoted in Table II correspond to this ambiguity. The total inefficiency due to the bremsstrahlung was estimated to be (1.2 ± 0.2)%.

Multitrack production: The signal events may have been discarded if more than two additional tracks were produced by interactions of electrons or associated photons in the detector materials. A study was carried out using a Bhabha sample, in which the requirement on the number of tracks was relaxed, but a very large total energy in LG was required. We visually investigated multitrack events in the sample, and found that the inefficiency due to the multitrack production was smaller than 0.05%.

Angular resolution: The finite resolution in the scattering angle measurement reduces the efficiency near the edge of the acceptance. This effect was evaluated by a simulation using the Monte Carlo sample. The scattering angles of the electrons were smeared according to the measured angular resolution, Eq. (2), and resultant decrease of the event yield (inefficiency) was counted. The result is listed in Table II, where the systematic error arising from the uncertainty in the resolution is added to the statistical error of the simulation. The inefficiency is significant only in the edge bins. The total inefficiency was (0.44 ± 0.06)%.

Angular accuracy: The polar angle of CDC tracks was measured from consistency between hits in the axial layers and the stereo layers. Errors in the wire-fix position along the beam axis may have resulted in a systematic shift of the measured angles. From surveys during the construction, we infer that the accuracy was better than 1 mm for the half length of the wires (1.5 m). However, a confirmation using the data is necessary since other unexpected errors may have had similar effects.

Position errors equivalent to systematic deformations of the endplates would result in a mismatch in the z intercepts or a mismatch in the scattering angles of two back-to-back tracks. The mismatch in the scattering angles of this sort can be distinguished from the effect of the beam-energy imbalance because of the different angular dependence. We found no significant mismatch in Bhabha scattering events, and set upper limits as $|\Delta\cot\theta/\cot\theta|<10^{-4}$ and $|\Delta\cot\theta|<10^{-3}$. From simulations, we found that possible effects of the allowed shifts are very small, less than 0.05% in the total yield.

On the other hand, those equivalent to the error in the total length of CDC are inaccessible by analyses of CDC alone. A study was carried out utilizing information from the barrel streamer tubes (BST). The track positions measured by BST were compared with the extrapolation of CDC tracks. The comparison was made for tracks in muon-pair events. We found no significant inconsistency and obtained an upper limit of $|\Delta\cot\theta/\cot\theta|<1.3\times10^{-3}$. The limit corresponds to a 2 mm uncertainty for the half-length of CDC. The corresponding total uncertainty in the event yield was estimated by the simulation to be 0.25%. The uncertainty in each angular bin is shown in Table II. The results for the backward four bins were ignored and set to zero, because they were fairly smaller than other errors and statistically insignificant.

The tilt of CDC with respect to the beam axis was not larger than 1 mrad, even if possible gradient of the beams with respect to the design orbit was taken into account. The effect of a tilt of this size is very small, less than 0.02% in the total yield.

Other tracking-related inefficiencies: The effect of the momentum resolution, Eq. (1), was very small because we set the momentum threshold very low. Turning the resolution on and off in the simulation altered the efficiency by only 0.02%. The effect of possible shifts of the momenta, which may have been caused by a systematic shift of the wire positions or an error in the magnetic field, was also very small. The relative shift $\Delta p_t/p_t$ was estimated to be smaller than 10^{-3} around the threshold. This estimate corresponds to an ambiguity in the detection efficiency at a level of 10^{-5}.

Particle motion inside the beam bunches and a possible energy imbalance between the incoming electron and positron may have resulted in certain effects similar to the tracking resolution and shifts. However, from the simulation, we found that their influence on the detection efficiency was smaller than 0.01%.

Dead LG modules: Since the LG array had no obvious gap within the angular coverage, dead modules were the

main source of the detection inefficiency in the calorimetry. We carried out light pulser tests employing xenon flash tubes (Xe tests) in order to monitor the response of the LG modules. Unrecoverable bad modules found in the tests were removed in the off-line analyses.

An event analysis was carried out to confirm the Xe-test results. A Bhabha event sample was selected by applying tight requirements on CDC tracks and one of the associated LG energy clusters. Then, we inspected those events in which neither of the CDC tracks was connected to any high-energy cluster (dead-module search). All 24 modules that had been removed prior to the start of the 1991 runs were found as candidates in this search.

Inspecting the response of candidate modules in all events, we found eight dead modules and four low-gain modules, in addition to the 24 removed modules. The eight dead modules died during the period relevant to the present analysis. Among them, six modules were dead only for the last 12% of the data. Among the four low-gain modules, two modules showed very small responses, less than 9 GeV, throughout the experiment. The other two modules were normal in earlier 25% of the data.

The inefficiency due to the identified dead modules was estimated by two methods. In the first method, we estimated the contributions of single dead modules by using a rotation method, in which a normal module at an azimuthally rotated position from a dead module was removed, and the resultant decrease of events in the Bhabha sample was counted. The inefficiency was evaluated by adding the contributions, according to the time-dependent list of the dead modules.

In the second method, the rotation method was applied to all known dead modules simultaneously, so that the inefficiency was directly evaluated. The estimation was carried out for several rotation angles. The two methods gave results consistent with each other. The discrepancy was smaller than 0.1%. The total inefficiency was from 0.8% to 1.1%, depending on the period. The inefficiency in each angle bin, estimated by the first method and averaged over the periods, is shown in Table II.

We visually inspected inefficient events found in the dead-module search. Though most of them were due to the identified dead modules, a certain number of events remained unidentified or ambiguous. The fraction of such events gives us an estimation on the reliability of the search. The errors quoted in Table II are the quadratic sum of the statistical error and the systematic error evaluated from the 90% confidence-level limit for the count of the ambiguous events. The total inefficiency averaged over the periods was $(0.8\pm0.1)\%$.

Abnormal response of LG: We were further concerned about the existence of unknown low-gain modules. A study was carried out using a response function of LG extracted from real data. We selected a purified Bhabha sample by tightening the acollinearity angle cut and the momentum cut in the event selection to 3° and 10 GeV/c, respectively. The association of a very high energy, larger than $0.8E_{\rm beam}$, was required with one of the tracks. The response function was extracted from the spectrum of the LG energy associated with the other track. The energies in the simulated events were then convoluted by the response function. Consequently, the change of the efficiency caused by the convolution was smaller than 0.01%. Namely, the effect of unknown low-gain LG modules was negligible, even if they existed.

TABLE III. Estimated background contamination in the barrel region.

	Contamination (%)			
Bin	Nonsignal $e^+e^-+n\gamma$	$\gamma\gamma$	$\tau^+\tau^-$	Multihadron
1	1.40 ± 0.20	0.66 ± 0.66	2.97 ± 0.49	0.07 ± 0.09
2	1.36 ± 0.20	0.41 ± 0.41	2.98 ± 0.49	0.13 ± 0.14
3	1.34 ± 0.19	0.30 ± 0.30	2.72 ± 0.45	0.18 ± 0.20
4	1.12 ± 0.16	0.22 ± 0.22	2.33 ± 0.39	0.17 ± 0.18
5	1.21 ± 0.17	0.17 ± 0.17	1.78 ± 0.30	0.27 ± 0.28
6	1.50 ± 0.19	0.14 ± 0.14	1.50 ± 0.25	0.21 ± 0.22
7	1.22 ± 0.15	0.11 ± 0.11	0.85 ± 0.15	0.13 ± 0.13
8	1.40 ± 0.16	0.08 ± 0.08	0.61 ± 0.11	0.05 ± 0.05
9	1.39 ± 0.16	0.06 ± 0.06	0.46 ± 0.08	0.08 ± 0.08
10	1.33 ± 0.14	0.05 ± 0.05	0.24 ± 0.04	0.05 ± 0.06
11	1.28 ± 0.13	0.03 ± 0.03	0.13 ± 0.02	0.02 ± 0.02
12	1.31 ± 0.13	0.02 ± 0.02	0.05 ± 0.01	0.01 ± 0.01

Other calorimetry-related inefficiencies: The effect of the energy resolution of LG was negligible. Even if the resolution was degraded to twice the nominal value in the simulation, the resultant change of the efficiency was only 0.02%. The effect of the error in the energy normalization was also negligible. We know that this error was not larger than 3%, from the response to the Bhabha events and the invariant mass of reconstructed neutral pions in multihadron events. The simulation showed that, even if there was a 10% error, it would cause an uncertainty of only 0.01% in the efficiency.

Trigger: The trigger inefficiency was negligible, since the event trigger was redundant for the Bhabha events in the barrel region. Triggers (i), (ii), (iii), and (iv) were simultaneously issued in most of the events. We found that the energy trigger (i) was issued in all selected events. The track trigger (iii), which was independent of trigger (i), was issued in 98% of the selected events. From these facts, we can estimate that the inefficiency of trigger (i) alone was already at a level of 10^{-5} or smaller.

3. Background contamination

Nonsignal $e^+e^-+n\gamma$: Consider those $e^+e^-+n\gamma$ events in which the e^+e^- pair satisfied the angle and track-momentum requirements in the selection but one of the electrons did not satisfy the energy requirement, $E\geqslant E_{\rm beam}/3$. They are not signal events, but may have been selected as the candidates, if a high-energy photon was emitted near to the low-energy electron (cluster coalescence). The contamination of such events was estimated by using the Monte Carlo sample. The estimated contamination is listed in Table III.

The uncertainty arising from ambiguities in the angular coverage and the angle measurement by LG was found to be smaller than 0.01% from simulations. Whereas, a sizable ambiguity is suspected in the theoretical calculation, since the calculation was at the tree level for $e^+e^-\gamma$ events. We assigned an overall error of 10% to the estimates. The errors quoted in Table III are the quadratic sum of the statistical error in the simulation and this systematic error. The total

contamination was estimated to be $(1.31\pm0.13)\%$.

Even if the electron pair did not satisfy the angular requirements, nonsignal $e^+e^-+n\gamma$ events could be present if a high-energy photon, emitted antiparallel to one of the electrons, converted in the detector materials. We estimated the production cross section of such events that would satisfy the selection criteria if the photon energy was used instead of the momentum of one of the electrons. The estimation was carried out using the TS program and another Tobimatsu-Shimizu program [28]. The latter generates those events in which one of the electrons escapes to small angles.

The cross section was estimated to be 4.6 pb. From this result, we can roughly estimate the contamination to be 0.14%, using the cross section of the signal of about 330 pb and the average photon conversion probability of 10%. The actual contamination must have been smaller, since the momenta of the conversion electrons are lower than the parent photons and the tracking capability would be bad for the conversion electrons. Therefore, we can expect the contamination of this type to be negligible, compared to the cluster-coalescence background.

$\gamma\gamma$: The $\gamma\gamma$ events could contaminate the Bhabha event sample if both photons converted. The total cross section of the $\gamma\gamma$ events is about 40 pb within $|\cos\theta|\leqslant0.743$ at $\sqrt{s}=58$ GeV. Multiplying the cross section with the average double-conversion probability of 1%, we obtain a rough estimate of the contamination of 0.4 pb, which corresponds to 0.12% of the signal. This must be an overestimation since the tracking capability would be bad for the conversion electrons. Indeed, a simulation including the detector effects gave an estimate of 0.03%. Conservatively, we estimated the total contamination to be $(0.06\pm0.06)\%$.

The contamination in each angular bin, estimated in the same way, is listed in Table III. Although the average is very small, the contamination is not negligible in backward bins since the angular dependence is quite different from Bhabha scattering events.

$\tau^+\tau^-$: The contamination from $\tau^+\tau^-$ events was estimated by using a Monte Carlo simulation, employing an event generator [29] followed by decays with JETSET 7.3 [30] and a full detector simulation. The decay branching ratios were updated to the Particle Data Group (PDG) values [31]. A total of 5000 events were generated and passed through the Bhabha selection. The estimated contamination was 0.43% of the Bhabha signal.

A possible error of the estimation was evaluated by changing the branching ratios. When we changed them within twice the errors quoted by PDG, the maximum variation of the contamination was 0.05%. We found in the simulation that most of the contaminating events included at least one τ decaying to the $e\nu\nu$ or $\rho\nu$ final state. Therefore, the ambiguity in the calorimeter energy normalization may cause a sizable error in the estimation. We estimated the uncertainty by changing the normalization by $\pm3\%$, and found that it resulted in a 0.03% change in the contamination.

Quadratically adding these uncertainties, we estimated the total contamination to be $(0.43\pm0.06)\%$. The estimated contamination in each angle bin is shown in Table III, where the statistical error of the simulation is added in quadrature. The contamination is as much as a few percent in backward bins, while it is negligible in the most forward bin.

Multihadron events: The contamination from the multihadron events was estimated to be 0.05% of the Bhabha signal by using a Monte Carlo simulation, JETSET 7.3 with patron shower [30] followed by a full detector simulation.

For a confirmation, we studied the number of low-momentum tracks in the Bhabha candidate events. We selected those events which had five or more tracks with a p_t threshold of 0.2 GeV/c. About 0.2% of the candidate events were such events, while more than 90% of the multihadron contamination was expected to remain. Among the selected events, one-half of the events had very large LG energies and were apparently Bhabha scattering events with shower-like interactions.

The remaining events, 0.1% of the Bhabha candidates, may have originated from multihadron production, though the $\tau^+\tau^-$ contribution seemed to be appreciable since the events showed negative forward-backward charge asymmetry. From these facts, we conservatively estimated the contamination of the multihadron events to be $(0.05\pm0.05)\%$. The contamination in each bin, estimated in the same way, is shown in Table III. The errors are the quadratic sum of the systematic error and the statistical error of the simulation.

Two-photon processes: The contamination from two-photon processes, $e^+e^-\rightarrow e^+e^-e^+e^-$, $e^+e^-\tau^+\tau^-$, and e^+e^-qq, was evaluated by using simulation samples generated according to the lowest-order QED cross section [32]. Applying the Bhabha selection to the samples, we found the total contamination was smaller than 0.05% of the Bhabha signal.

C. Results

The errors associated with the corrections described above have a certain correlation between angular bins. Such a correlation can be handled by means of the error (covariance) matrix technique. The error matrix is determined as

$$C_{ij}=\sum_k \Delta_i^{(k)}\Delta_j^{(k)}, \tag{3}$$

where k runs over all independent components of the error. The factor $\Delta_i^{(k)}$ is the nominal (one standard-deviation) shift of the result in the ith bin, corresponding to the kth error component. If the kth component is relevant to the ith bin alone, such as a statistical error, $\Delta^{(k)}$ is nonzero for the ith bin only.

The total error in the ith bin is given by the diagonal component of the error matrix as

$$\Delta_i=\sqrt{C_{ii}}, \tag{4}$$

and the error of the total sum is given by

$$\Delta_{\text{total}}=\sqrt{\sum_{i,j} C_{ij}}. \tag{5}$$

The correlation matrix (ρ_{ij}) is defined as

$$C_{ij}=\rho_{ij}\Delta_i\Delta_j. \tag{6}$$

By the definition, diagonal elements of ρ_{ij} are all unity and $\rho_{ji}=\rho_{ij}$.

TABLE IV. Nondiagonal elements of the correlation matrix (ρ_{ij}) for the errors of N_i and R_i in Table I. This is valid also for the errors of R_i^{EB} and $dR^{\mathrm{EB}}/d\Omega$ in Table V.

Bin	1	2	3	4	5	6	7	8	9	10	11
2	0.065										
3	0.056	0.053									
4	0.051	0.049	0.046								
5	0.044	0.044	0.043	0.042							
6	0.046	0.044	0.043	0.040	0.043						
7	0.035	0.035	0.035	0.034	0.038	0.052					
8	0.034	0.033	0.032	0.031	0.032	0.038	0.038				
9	0.038	0.038	0.038	0.023	0.046	0.051	0.053	0.056			
10	0.038	0.039	0.008	0.039	0.051	0.057	0.064	0.069	0.104		
11	0.043	0.017	0.042	0.042	0.058	0.071	0.080	0.090	0.138	0.182	
12	0.035	0.050	0.048	0.047	0.063	0.091	0.090	0.105	0.159	0.206	0.293

The number of signal events (N_i) corrected for the detection inefficiency and the background contamination is listed in Table I. The errors are the sum of the statistical error of n_i and the systematic errors shown in Table II and Table III, evaluated from the error matrix according to Eq. (4). Note that one item of the correction often contained several independent sources of the error, as described in previous subsections. Estimated nondiagonal elements of the correlation matrix are presented in Table IV. The correlation is significant between forward bins. The elements $\rho_{1,12}$, $\rho_{2,11}$, $\rho_{3,10}$, and $\rho_{4,9}$ are relatively small because of the presence of a negative correlation in the error of the charge misidentification probability.

Using Eq. (5), the total inefficiency was estimated to be $(4.06\pm0.36)\%$ and the total background contamination was $(1.86\pm0.17)\%$. These corrections lead to a total number of signal events of $(9.818\pm0.050)\times10^4$, where the error includes the statistical error (0.3%) as well.

The distributions of the acollinearity angle, track momenta and associated LG energies of the candidate events are shown in Figs. 3–5. The corresponding results from simulations, Bhabha scattering events including the cluster-coalescence background plus the $\tau\tau$ and multihadron contamination, are overwritten with histograms. The $\tau\tau$ and multihadron contamination, which is separately shown with hatched histograms, is the result of a full detector simulation and normalized to the approximate luminosity. The Bhabha events generated by the TS program were smeared according to the bremsstrahlung formula and detector resolutions, and are normalized to the total number of events.

In the acollinearity angle distribution (Fig. 3), a disagreement can be seen at very small angles. This is attributed to an effect of the multiple photon emission, ignored in the simulation. This is not a problem since the agreement is satisfactory at large angles near the cut value.

The measurement and simulation are in good agreement in the momentum distribution (Fig. 4). Discrepancies are observed only in high-momentum regions, far away from the threshold. The shift of the peak position in Fig. 4(b) is due to a non-Gaussian behavior of the momentum resolution in the data. The peak position depends on such details because the distributions in Fig. 4 are biased by the selection of the lower and higher momentum tracks. Unbiased distributions, e.g, p/E_{beam} do not exhibit such a shift. On the other hand, the momentum resolution is not an issue at low momenta near the threshold. The good agreement at low momenta shows that the applied simulation of the bremsstrahlung, which played an important role in the estimation of the efficiency, is reliable.

We can see apparent discrepancies in the LG energy distributions. The discrepancies at high energies are due to an unrealistic energy resolution assumed in the simulation; e.g., non-Gaussian tails are not taken into consideration. The disagreement at medium energies in Fig. 5(b) is mainly due to an inaccurate simulation of shower overlaps.

In the simulation, we assumed that deposits having opening angles smaller than 5°, which is comparable with a typical size of one LG module, were merged to one energy cluster. The result from another simulation, in which the merge angle was narrowed to 1°, is shown with dotted histograms for a comparison. We can see that the population of Bhabha events steeply decreases at small energies, $E_{\mathrm{lower}}<E_{\mathrm{beam}}/2$, regardless of the details of the simulation. This is the reason

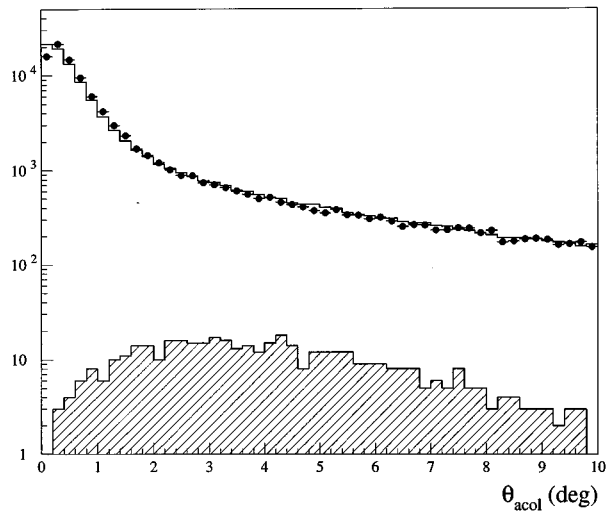

FIG. 3. Acollinearity angle distribution of the candidate events in the barrel region. The histogram shows the expectation from a simulation, including both the signal and the background. The estimated contamination from the $\tau\tau$ and multihadron events is shown with the hatched histogram. The simulation for the Bhabha-scattering events is normalized to the total yield.

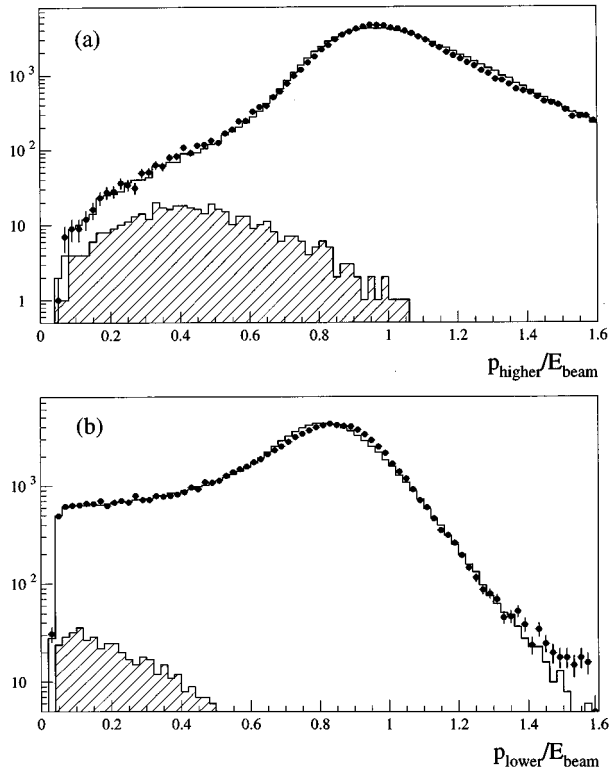

FIG. 4. Momentum distribution of the CDC tracks of the candidate events in the barrel region. The distribution is shown for (a) the higher-momentum track and (b) the lower-momentum track, separately. The definition of the histograms is the same as Fig. 3.

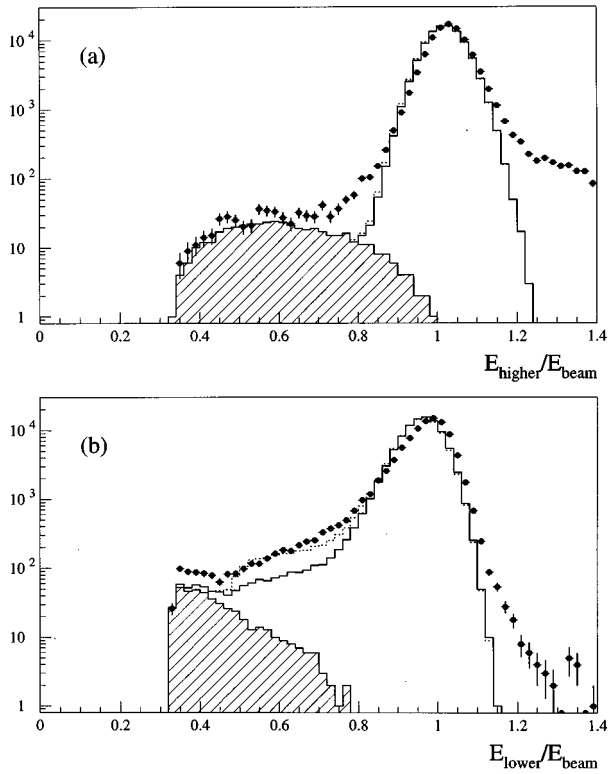

FIG. 5. Distribution of the LG energies of the candidate events in the barrel region. The distribution is shown for (a) the higher-energy cluster and (b) the lower-energy cluster, separately. The definition of the solid histograms is the same as Fig. 3. The dashed histograms show the result from another simulation, where electromagnetic showers in LG are assumed to be merged to one cluster if the opening angle is smaller than 1°, instead of the standard assumption of 5°.

why the detection efficiency is insensitive to the detailed characteristics of LG.

The discrepancy that we can see near the threshold in Fig. 5(b) could be serious, since it cannot be recovered by a fine-tuning in the simulation. We selected those events which exhibited very low energies, $E_{\rm lower}/E_{\rm beam}<0.45$, and investigated the spectrum of $E_{\rm higher}$. The obtained spectrum is shown in Fig. 6, together with the corresponding simulation result. The signal and the background are clearly separable in this spectrum. In a background dominant region, $E_{\rm higher}/E_{\rm beam}<0.8$, the measurement is in good agreement with the simulation. Observed discrepancy in this region (8%) is smaller than the systematic error estimated for the $\tau\tau$ and multihadron contamination.

On the other hand, a discrepancy is apparent in a higher energy region in Fig. 6. From a visual inspection, we found that this was due to an effect of dead LG modules, where one of the electrons hit the LG array close to one of the dead modules. Such effects were not taken into account in the simulation. However, this is not a problem since the dead-module effects were evaluated using real data.

IV. ANALYSIS IN THE END-CAP REGION

A. Event selection

The event selection can be simpler in the forward (end-cap) region since the background is less severe. The selections applied were based on information from the end-cap calorimeters (LA) alone. We required that at least one pair of high-energy ($E\geq E_{\rm beam}/3$) and collinear ($\theta_{\rm acol}\leq 4°$) LA-energy clusters be observed in an angular region of $0.822\leq|\cos\theta|\leq 0.968$. The scattering angle ($\theta$) was determined from the shower-center position measured by LA, as-

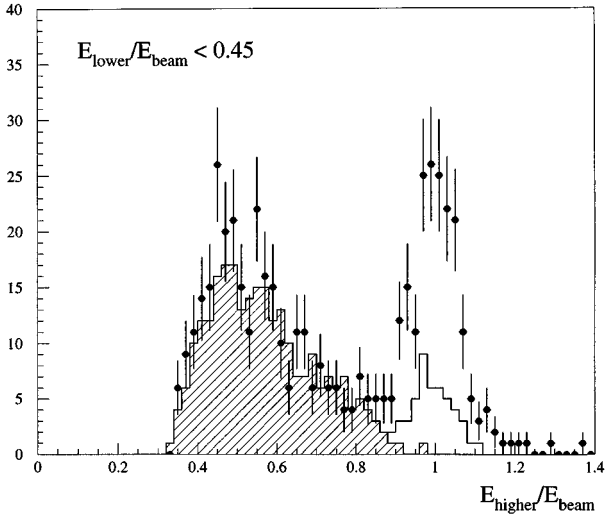

FIG. 6. Distribution of the higher LG energy in those events which exhibit very low energies, $E_{\rm lower}/E_{\rm beam}<0.45$, in Fig. 5(b). The definition of the histograms is the same as Fig. 3.

suming that the particles originated from the center of the detector.

The inner edge of the acceptance corresponds to the boundary between ring 2 and ring 3 of LA, and the outer edge corresponds to the boundary between ring 9 and ring 10. The requirement on the collinearity was chosen to be tighter than in the barrel region, so as to avoid contamination from collisions of satellite beam bunches. A total of 1045.1×10^3 events were selected.

B. Corrections

1. Definition of the signal

In the end-cap region, the signal was defined to be those events from the reaction $e^+e^-\rightarrow e^+e^-+n\gamma$ ($n=0,1,\ldots,\infty$), in which both e^+ and e^- scattered to a forward region ($14.53°\leqslant\theta\leqslant34.71°$), both had large energies ($E\geqslant E_{\rm beam}/3$) and the acollinearity angle between them was smaller than 4°. The backward scattering was treated as background.

2. Detection efficiency

Shower fluctuation: The angular acceptance was blurred by the fluctuation of the shower development in LA and materials placed in front of it. Corresponding changes in the event yield were evaluated by applying a full detector simulation of Monte Carlo events generated by the TS program [7]. The distributions of known materials, such as the structure and support of the detector components, were all implemented in the simulation. However, certain ambiguities remained in the distribution of some materials at small angles, such as readout electronics and cables of the vertex chamber and the trigger chamber. In the simulation, these materials were modeled with cylinders placed at appropriate positions. The thicknesses of the cylinders were tuned so that the simulated energy response of LA reasonably reproduced the measurements.

From the simulation, we found a decrease in the Bhabha-event yield (inefficiency) due to the shower fluctuation of (0.8 ± 0.4)%. The error is dominated by the ambiguity in the material distribution. The measured energy spectrum of LA for the electrons in Bhabha events is plotted in Fig. 7. The solid histogram shows the spectrum from the simulation under the optimum setting. The other histograms correspond to the minimum and maximum thicknesses of the materials that we assumed in the error estimation. The measurement shows a wider spectrum than those of the simulations, indicating a non-uniform distribution of materials. We can see that the full range of the assumption about the thickness covers the non-uniformity.

It should be noted that the effect of the shower loss itself on the detection efficiency was negligible, since the energy threshold was set very low. The inefficiency was caused by the lateral shower fluctuation of electrons scattered near to the inner edge of the acceptance.

Spread of the interaction point: The spread of the interaction point causes a decrease of the acceptance. Since the lateral spread was very small, what we should be concerned about is the longitudinal spread of 1.0 cm. A naive simulation, in which the error in the position measurement was treated as an independent Gaussian fluctuation, showed a decrease in the Bhabha event yield of 0.3%.

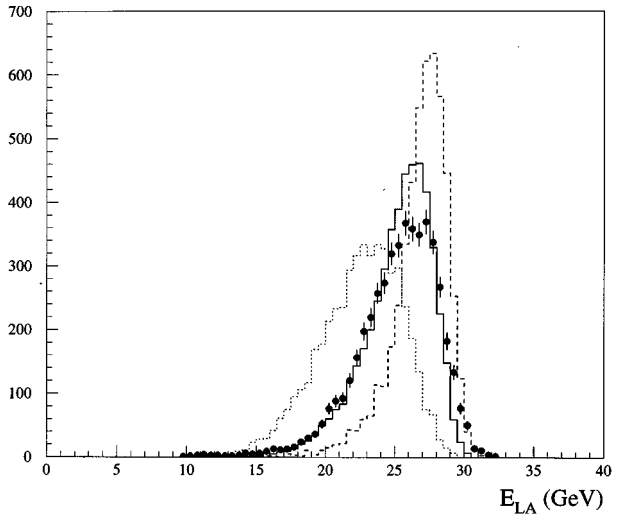

FIG. 7. Energy response of LA for the electrons in Bhabha events. The sum of the energies observed in rings 3 and 4 in each counter is plotted. The solid histogram shows the simulation result under the optimum setting of the material distribution. The other histograms correspond to the minimum and maximum thicknesses of materials that we imposed in the error estimation. The simulation results are normalized to the total yield.

On the other hand, the full detector simulation showed a 0.5% increase in the yield when we added the longitudinal spread. Since a reasonable decrease was observed when we enlarged the spread, the difference is attributed to an effect of a correlation in the position measurement ignored in the naive simulation. Consequently, we adopted the estimation from the full simulation and, for safety, added one-half of the discrepancy from the naive simulation (0.4%) to the systematic error, since the mechanism was not clearly understood.

Placement of the LA counters: Accurate information on the placement of the LA counters was crucial in order to precisely determine the acceptance. The placement error was measured from inconsistencies between measured positions of two electrons in Bhabha scattering events. A study was also carried out by comparing the positions with the extrapolation of CDC tracks at larger angles. Both measurements gave consistent results, despite the fact that they used information in different angular regions.

From these measurements, we found an overall transverse displacement of the LA system of 3.9 ± 1.1 mm with respect to the beam line, a relative transverse displacement between the counters of 4.2 ± 1.6 mm, and a parallel displacement along the beam line of 2.6 ± 0.8 mm with respect to the average interaction point. Furthermore, the distance between the counters was found to be shorter by 7.6 ± 5.0 mm than the design value. The error in the distance is dominated by the ambiguity in the angle measurement by CDC.

The naive simulation and the full simulation gave a consistent estimation of the inefficiency due to the displacements. The estimated inefficiency was (0.8 ± 0.3)%. Note that the effects of the placement errors, except for the error in the distance, were smeared by the shower fluctuation and the interaction point spread, whose effects were already taken into account.

Dead channels: Another source of inefficiency was the dead channels of LA. Dead channels were found by inspecting hit maps in representative periods of the experiment. A total of 46 channels were dead at the start of the 1991 runs. They increased to 132 channels at the end of the experiment. However, since LA had four longitudinal segments and the main part of the electromagnetic energy was deposited in the first two segments, the effect was negligible even if the third and fourth segments were dead. The number of modules in which both the first and second segments were dead was 11 at the end of the experiment. Either the first or second segment was dead in 12 modules.

The inefficiency due to the dead channels was estimated by adding contributions of single modules (one-module contributions), taking into account the time dependence of the dead-channel distribution. The one-module contributions were evaluated using the collected Bhabha scattering events by means of a rotation method similar to that applied to the LG modules. The evaluation was carried out for typical patterns of dead segments in the modules.

The estimated inefficiency, averaged over the relevant experimental period, was $(1.27\pm0.24)\%$. The error includes the uncertainty in the estimation of the one-module contributions and in the time dependence. The estimation was confirmed by another analysis in which the rotation was applied to all dead channels simultaneously.

Trigger: The candidate events were mainly triggered by the LA total-sum trigger (v). The trigger efficiency was studied by using a preselection sample for a study of multihadron production. Recorded information on trigger (v) was investigated in those events which were triggered by at least one of the other triggers. The analysis was applied to the sample selected from all 58 GeV data since 1991. We found that trigger (v) was issued in all 2110 events that had large energy deposits, larger than 1/3 of the beam energy, in both LA counters. The result suggests that the inefficiency was at most 0.1% and negligible compared to other errors.

The estimation was confirmed by another study, where we inspected the individual trigger information from the two LA counters recorded in the Bhabha candidate events. The efficiency could be crosschecked since events were triggered if either counter issued the trigger signal. We inspected nearly one-half of the candidates (about 440k events) in representative periods, and found no loss of the trigger signal in both counters. This indicates that the trigger inefficiency was far smaller than 0.1%.

3. Background contamination

Since the Bhabha-scattering cross section is very large in the end-cap region, the background was dominated by non-signal $e^+e^-+n\gamma$ events. The contamination of these events was estimated by using the TS programs [7,28] and found to be 2.0% of the signal. Among them, the contribution of the backward scattering was only 0.14%. The other part was the contribution of $e^+e^-\gamma$ events in which the photon was misidentified as an electron. The ambiguity due to the shower overlap was smaller than 0.1%. Taking possible higher-order contributions into consideration, we estimated the contamination of non-signal $e^+e^-+n\gamma$ events to be $(2.0\pm0.2)\%$.

The $\gamma\gamma$ events were not separated from the e^+e^- events in the event selection. Their contamination was estimated by using a $\gamma\gamma$ event generator [33] to be $(1.56\pm0.05)\%$ of the obtained candidates, where the estimation was normalized to the approximate luminosity with an uncertainty of 2.7%. The contamination from the $\tau^+\tau^-$ and multihadron production was negligible; both were at the 0.01% level.

C. Results

From the estimation described above, we evaluated the total inefficiency to be $(2.4\pm0.7)\%$ with a total background contamination of $(3.6\pm0.2)\%$. These estimates lead us to a corrected number of signal events in the end-cap region ($N_{\rm EC}$) of $(1032.6\pm7.3)\times10^3$.

V. PHYSICS DISCUSSIONS

A. Model-independent angular distribution

In order to compare the measurements with theoretical predictions, we define a normalized angular distribution (R_i) as

$$R_i \equiv \frac{N_i}{N_{\rm EC}} = \frac{\sigma_i}{\sigma_{\rm EC}}, \tag{7}$$

where σ_i is the integrated cross section in the ith angular bin of the barrel region and $\sigma_{\rm EC}$ is the total cross section in the end-cap region, to be evaluated according to the definition of the signal in each region. The quantity R_i is independent of any specific theory or model since no theoretical unfolding is applied. The obtained R_i distribution is presented in Table I. This is the primary result of the experiment, from which all numerical results are extracted in the following physics discussions. Note that the quoted errors do not include the overall normalization error of 0.7% arising from the measurement in the end-cap region. It is otherwise taken into account in numerical evaluations.

B. Comparison with the standard electroweak theory

The prediction of the standard electroweak theory for the R_i distribution was calculated by using a computer program ALIBABA [9]. ALIBABA includes the exact first-order photon-radiation correction and a dominant part (leading-log part) of the second-order corrections, as well as internal electroweak loop corrections. Further higher orders of the photon-radiation corrections are partly included by an exponentiation. Other programs [10] including second-order photon-radiation corrections are not adequate for the present use. They use approximations which are appropriate for the Z^0 resonance region but lead to appreciable inaccuracies at TRISTAN energies.

The prediction is shown in the last column of Table I [34]. Input physical parameters of ALIBABA, the masses of Z^0, the top quark and the Higgs boson, were chosen to be 91.19, 170, and 300 GeV/c^2, respectively. The ratio of the measurement to the prediction $[R_i/R_i(\rm EW)]$ is plotted in Fig. 8. The error bars correspond to the total error presented in Table I while inner ticks marked on the bars show the contribution of the statistical error alone. The latter dominates in all bins. The normalization error arising from the error of $N_{\rm EC}$ (0.7%) is indicated by the dashed lines. No significant deviation from unity can be found.

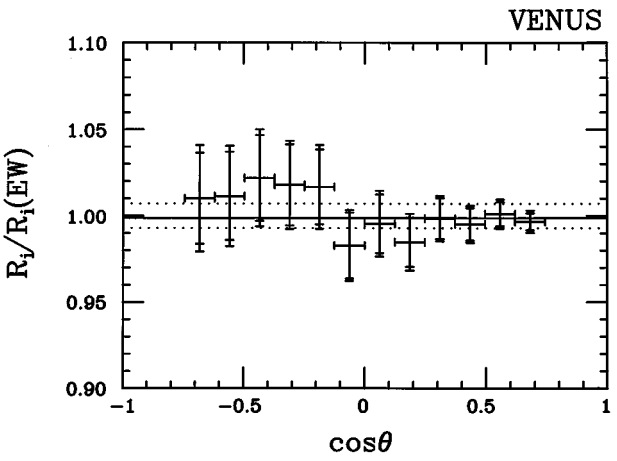

FIG. 8. Measured model-independent scattering angle distribution, $R_i=\sigma_i/\sigma_{\rm EC}$, normalized to the prediction from the standard electroweak theory. The prediction was calculated using ALIBABA. The inner ticks on the error bars represent the contribution of the statistical error. The error bars do not include the normalization error arising from the measurement in the end-cap region. The range of the normalization error (0.7%) is indicated with dotted lines. The solid line indicates the optimum normalization determined by the fit.

For numerical evaluations of the consistency, we defined a χ^2 as follows:

$$\chi^2=\sum_{i,j=1}^{12} C_{ij}^{-1}(ax_i-x_i^0)(ax_j-x_j^0)+\frac{(a-1)^2}{\Delta_a^2}, \qquad (8)$$

where x_i^0 denotes a prediction for the quantity x_i; here, $x_i=R_i$. The overall normalization is allowed to vary by introducing a free parameter a, with a constraint of $\Delta_a=\Delta N_{\rm EC}/N_{\rm EC}=0.007$. The error matrix C_{ij} is given by the error of the measurement x_i and the correlation matrix ρ_{ij} in Table IV. This definition is used in all numerical evaluations in the following discussions, unless noted otherwise.

The minimum χ^2 obtained by the fit was 3.85 for 12 degrees of freedom, with $a=1.0012\pm0.0041$. Namely, the measurement and the prediction are in excellent agreement. The solid line in the figure indicates the best fit. It should be noted that all corrections applied in the analyses were established before comparing with the prediction. Therefore, the result is expected to be free from any artificial biases.

In the following subsections, we examine the sensitivity of the present experimental result to theories and models composing the standard theory. We also investigate how tightly possible alternations of the standard theory and hypothetical new interactions are constrained by the present result.

C. Normalized effective-Born cross section

The cross sections of reactions in e^+e^- collisions can be described by kernel (effective Born) cross sections and a photon-radiation correction applied to it by convolutions [35]. The photon-radiation correction comprises a minimum gauge-invariant subset of QED corrections including external photon emissions; i.e., photonic vertex and box corrections are included as well. Other internal loop corrections in the standard electroweak theory, propagator corrections, and pure-weak vertex and box corrections, can be enclosed in the kernel.

As a consequence, the cross sections relevant to our measurement can be factorized as

$$\sigma_i=\sigma_i^{\rm EB}(1+\delta_i^{\rm rad}), \qquad (9)$$

where $\sigma_i^{\rm EB}$ is the effective-Born cross section integrated over the bin and $\delta_i^{\rm rad}$ is the average photon-radiation correction. Since $\sigma^{\rm EB}$ corresponds to a two-body elastic reaction, $e^+e^-\to e^+e^-$, it is only a function of the c.m. energy ($\sqrt{s}$) and the scattering angle (θ). Therefore, theoretical calculations are more straightforward than those for σ_i. All other experimental constraints are absorbed in the correction $\delta^{\rm rad}$. Further, $\sigma^{\rm EB}$ can be extracted experimentally without any theoretical assumptions, except for the validity of QED assumed in the determination of $\delta^{\rm rad}$. Thus, comparisons with theories can be performed with less theoretical biases than those using tree-level (Born) cross section.

In analogy to Eq. (9), we defined a number of events in the effective-Born scheme ($N_i^{\rm EB}$) as

$$N_i=N_i^{\rm EB}(1+\delta_i^{\rm rad}), \qquad (10)$$

and redefined a normalized angular distribution as

$$R_i^{\rm EB}\equiv\frac{N_i^{\rm EB}}{N_{\rm EC}^{\rm EB}}=\frac{\sigma_i^{\rm EB}}{\sigma_{\rm EC}^{\rm EB}}. \qquad (11)$$

The photon-radiation correction ($\delta_i^{\rm rad}$) was evaluated from σ_i and $\sigma_i^{\rm EB}$ given by ALIBABA. The numerical results on $\delta_i^{\rm rad}$ and $R_i^{\rm EB}$ are listed in Table V. The accuracy of $\delta_i^{\rm rad}$ is anticipated to be better than 0.5%, although it is not included in the errors.

For further convenience, the obtained $R_i^{\rm EB}$ distribution was converted to a normalized differential cross section at the center ($\cos\theta_i$) of the $\cos\theta$ bins as

$$\frac{dR^{\rm EB}(\cos\theta_i)}{d\Omega}\equiv\frac{R_i^{\rm EB}}{2\pi\Delta\cos\theta(1+\delta_i^{\rm bin})}=\frac{1}{\sigma_{\rm EC}^{\rm EB}}\frac{d\sigma^{\rm EB}(\cos\theta_i)}{d\Omega}, \qquad (12)$$

where $\Delta\cos\theta$ is the bin width. The correction for the binning effect ($\delta_i^{\rm bin}$), the difference between the average and the center value, was determined from the effective-Born cross section given by ALIBABA. The numerical result is presented in Table V, together with the prediction from ALIBABA.

D. Improved-Born approximation to the standard theory

It is well known that, within the standard electroweak theory, the internal loop corrections can be reproduced, with a good precision, by applying the following replacements to the Born cross section (improved-Born approximation) [35]:

$$\alpha\to\alpha(q^2)=\frac{\alpha}{1-\Delta\alpha(q^2)}, \qquad (13)$$

TABLE V. Scattering angle distributions in the effective-Born scheme. The distribution R_i has been converted to $R_i^{\rm EB}$ by unfolding the photon-radiation correction $\delta_i^{\rm rad}$. The distribution is further converted to the normalized differential cross section ($dR^{\rm EB}/d\Omega$) at the center of the bins quoted in the second column. The prediction from the standard electroweak theory [$dR^{\rm EB}({\rm EW})/d\Omega$] is shown for a comparison. The errors do not include the normalization error (0.7%) from the measurement in the end-cap region.

Bin	$\cos\theta_i$	$\delta_i^{\rm rad}$	$R_i^{\rm EB}$ (10^{-3})	$dR^{\rm EB}/d\Omega$ (10^{-3})	$dR^{\rm EB}({\rm EW})/d\Omega$ (10^{-3})
1	−0.681	−0.180	1.520±0.047	1.952±0.060	1.932
2	−0.557	−0.140	1.568±0.045	2.012±0.058	1.989
3	−0.433	−0.142	1.686±0.046	2.163±0.060	2.116
4	−0.310	−0.141	1.860±0.047	2.384±0.060	2.342
5	−0.186	−0.142	2.153±0.052	2.758±0.066	2.713
6	−0.062	−0.140	2.538±0.053	3.247±0.068	3.304
7	0.062	−0.138	3.312±0.063	4.232±0.081	4.251
8	0.186	−0.133	4.485±0.075	5.720±0.096	5.809
9	0.310	−0.128	6.669±0.088	8.480±0.112	8.494
10	0.433	−0.118	10.61±0.12	13.42±0.15	13.49
11	0.557	−0.110	19.09±0.16	23.94±0.20	23.92
12	0.681	−0.155	40.87±0.26	50.22±0.32	50.39
EC		−0.126			

$$\frac{\alpha}{16\sin^2\theta_W\cos^2\theta_W}\rightarrow\alpha_Z(q^2)=\frac{G_F M_Z^2}{8\sqrt{2}\pi}\,\rho(q^2), \tag{14}$$

$$\frac{g_\nu}{g_a}=1-4\sin^2\theta_W\rightarrow r_V=1-4\sin^2\theta_W^{\rm eff}, \tag{15}$$

$$\Gamma_Z\rightarrow\frac{s}{M_Z^2}\,\Gamma_Z. \tag{16}$$

The correction to the fine-structure constant, originating from the self-energy (vacuum polarization) corrections to the photon propagator, can be separated to a leptonic part and a hadronic part, i.e.,

$$\Delta\alpha(q^2)=\Delta\alpha_{\rm lep}(q^2)+\Delta\alpha_{\rm had}(q^2). \tag{17}$$

The leptonic part can be calculated perturbatively as

$$\Delta\alpha_{\rm lep}(q^2)=\frac{\alpha}{3\pi}\sum_{l=e,\mu,\tau}\left[\ln\frac{|q^2|}{m_l^2}-\frac{5}{3}\right]. \tag{18}$$

On the other hand, the hadronic part is usually evaluated from a dispersion relation, utilizing measurements of the $e^+e^-\rightarrow$hadrons reaction, because of a presence of strong non-perturbative effects. Burkhardt *et al.* [36] found that the hadronic part can be approximated in the form of

$$\Delta\alpha_{\rm had}(q^2)=A+B\,\ln(1+C|q^2|). \tag{19}$$

From their numerical results, they gave the parameters as $A=0.001\,65$, $B=0.003$, and $C=1.0\ {\rm GeV}^{-2}$ in a large q^2 region, $|q^2|>(3\ {\rm GeV})^2$, in which the present measurement is all contained.

The deviation of $\rho(q^2)$ from the unity is negligible, compared to the measurement accuracy. The nonunity effect is smaller than 0.1% at any scattering angle. Other parameters have been determined very precisely by low-energy experiments [31] and experiments at the CERN e^+e^- collider LEP and SLAC linear collider (SLC) [4].

Under this approximation, the ten terms of the Bhabha-scattering cross section, individual contributions of the four diagrams plus six interferences between them, can be written as

$$\left(\frac{d\sigma^{\rm IB}}{d\Omega}\right)_{\gamma_t\gamma_t}=\frac{1}{4s}\,\alpha(t)^2 2\,\frac{(1+\cos\theta)^2+4}{(\cos\theta-1)^2},$$

$$\left(\frac{d\sigma^{\rm IB}}{d\Omega}\right)_{\gamma_s\gamma_t}=\frac{1}{4s}\,\alpha(s)\alpha(t)2\,\frac{(1+\cos\theta)^2}{\cos\theta-1},$$

$$\left(\frac{d\sigma^{\rm IB}}{d\Omega}\right)_{\gamma_s\gamma_s}=\frac{1}{4s}\,\alpha(s)^2(1+\cos^2\theta),$$

$$\left(\frac{d\sigma^{\rm IB}}{d\Omega}\right)_{\gamma_t Z_s}=\frac{1}{4s}\,\frac{s(s-M_Z^2)\alpha(t)\alpha_Z(s)}{(s-M_Z^2)^2+(s\Gamma_Z/M_Z)^2}\,2(1+r_V^2)\,\frac{(1+\cos\theta)^2}{\cos\theta-1},$$

$$\left(\frac{d\sigma^{\rm IB}}{d\Omega}\right)_{\gamma_t Z_t}=\frac{1}{4s}\,\frac{s\alpha(t)\alpha_Z(t)}{t-M_Z^2}\,\frac{2}{\cos\theta-1}\,\{(1+r_V^2)(1+\cos\theta)^2-4(1-r_V^2)\},$$

$$\left(\frac{d\sigma^{\rm IB}}{d\Omega}\right)_{\gamma_s Z_s} = \frac{1}{4s}\frac{s(s-M_Z^2)\alpha(s)\alpha_Z(s)}{(s-M_Z^2)^2+(s\Gamma_Z/M_Z)^2}\,2\{r_V^2(1+\cos^2\theta)+2\cos\theta\},$$

$$\left(\frac{d\sigma^{\rm IB}}{d\Omega}\right)_{\gamma_s Z_t} = \frac{1}{4s}\frac{s\alpha(s)\alpha_Z(t)}{t-M_Z^2}\,(1+r_V^2)(1+\cos\theta)^2,$$

$$\left(\frac{d\sigma^{\rm IB}}{d\Omega}\right)_{Z_s Z_s} = \frac{1}{4s}\frac{s^2\alpha_Z(s)^2}{(s-M_Z^2)^2+(s\Gamma_Z/M_Z)^2}\,\{(1+r_V^2)(1+\cos^2\theta)+8r_V^2\cos\theta\},$$

$$\left(\frac{d\sigma^{\rm IB}}{d\Omega}\right)_{Z_s Z_t} = \frac{1}{4s}\frac{s^2(s-M_Z^2)\alpha_Z(s)\alpha_Z(t)}{\{(s-M_Z^2)^2+(s\Gamma_Z/M_Z)^2\}(t-M_Z^2)}\,[(1+r_V^2)^2+4r_V^2](1+\cos\theta)^2,$$

$$\left(\frac{d\sigma^{\rm IB}}{d\Omega}\right)_{Z_t Z_t} = \frac{1}{4s}\frac{s^2\alpha_Z(t)^2}{(t-M_Z^2)^2}\frac{1}{2}\,\{[(1+r_V^2)^2+4r_V^2](1+\cos\theta)^2+4[(1+r_V^2)^2-4r_V^2]\}, \tag{20}$$

where $t=-s(1-\cos\theta)/2$. This approximation, with the parameters of $M_Z=91.19$ GeV/c^2, $\Gamma_Z=2.49$ GeV, and $\sin^2\theta_W^{\rm eff}=0.232$, well reproduces the effective-Born cross section given by ALIBABA. The precision is better than 0.1% at all scattering angles.

E. Running of α

The running of α, i.e., the photon vacuum polarization, was treated as a part of well-known QED corrections in PEP/PETRA and early TRISTAN experiments [1–3], even though it includes an ambiguous hadronic contribution. Recently, the TOPAZ group studied the running effect explicitly by using their multihadron production data [37]. Though the normalization point of q^2 is not explicitly specified, their result shows the effect with a significance of about three standard deviations.

In order to examine this effect, we compared the measured angular distribution ($dR^{\rm EB}/d\Omega$) with the prediction from an improved-Born approximation without the $\Delta\alpha(q^2)$ correction, $dR^{\rm IB}$ (fixed α)/$d\Omega$. The ratio is plotted in Fig. 9. The solid curve in the figure represents the prediction under the standard setting; i.e., it is equivalent to the prediction of the standard theory. The approximation including only the leptonic correction is shown with the dashed curve. The latter falls below the data, indicating a sensitivity not only to the total $\Delta\alpha(q^2)$ contribution, but also to the contribution of the hadronic part ($\Delta\alpha_{\rm had}$). It should be noted that the angular distribution of Bhabha scattering reflects the running behavior in a wide range of q^2, since q^2 of the t-channel photon propagator varies with the scattering angle.

A numerical evaluation was tried by using expression (19), together with Eqs. (17), (18), and (20). Since the experimental result $dR^{\rm EB}/d\Omega$ is a ratio of the cross section, it is not sensitive to the absolute value of α, thus to the parameter A in Eq. (19). In addition, the measurement is relatively insensitive to C, since $C|q^2|$ is expected to be fairly larger than 1. Hence, we carried out a fit to the experimental result ($dR^{\rm EB}/d\Omega$) by setting $A=0$ and $C=1.0$ GeV^{-2}, with the parameter B left free. The best fit was

$$B=0.0030\pm0.0017. \tag{21}$$

In the end-cap region, the cross section is dominated by the t-channel photon exchange, with an average $|t|$ of (10 GeV)^2. Therefore, assuming the form of Eq. (19), what we have measured can be expressed as

$$\Delta\alpha_{\rm had}[(57.77\ \ {\rm GeV})^2]-\Delta\alpha_{\rm had}[(10\ \ {\rm GeV})^2] = 0.0105\pm0.0059. \tag{22}$$

If we add the leptonic contribution, Eq. (18), this leads to

$$\Delta\alpha[(57.77\ \ {\rm GeV})^2]-\Delta\alpha[(10\ \ {\rm GeV})^2]=0.0186\pm0.0059. \tag{23}$$

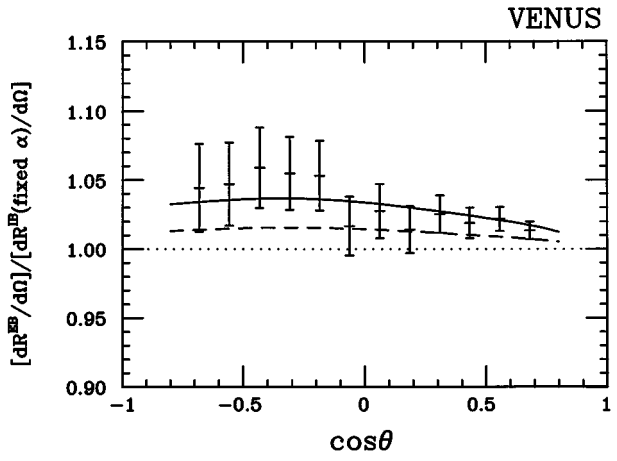

FIG. 9. Measured radiation-unfolded scattering angle distribution, $dR^{\rm EB}/d\Omega=(d\sigma^{\rm EB}/d\Omega)/\sigma_{\rm EC}^{\rm EB}$, normalized to the prediction from the improved-Born approximation with fixed α. The non-zero excess from the unity reflects the q^2-running effect of α. The expectation from the standard improved-Born approximation, equivalent to the standard theory prediction, is shown with the solid curve. The dashed curve shows the approximation including the leptonic correction only.

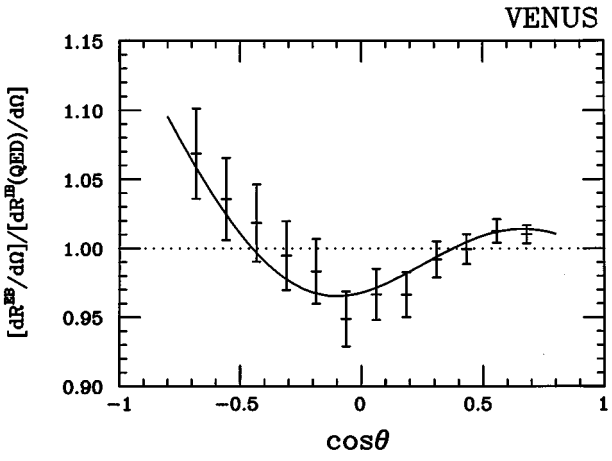

FIG. 10. Measured radiation-unfolded scattering angle distribution, $dR^{\mathrm{EB}}/d\Omega$, normalized to the prediction from the improved-Born approximation for the QED contribution (photon exchanges only). The expectation from the standard improved-Born approximation, equivalent to the standard theory prediction, is shown with the solid curve.

Consequently, the hadronic contribution to the q^2 running of α has been directly observed in a large $|q^2|$ region, $|q^2|>$ $(3\ \mathrm{GeV})^2$, with a significance of about two standard deviations. Furthermore, the expected q^2 running of α, including the leptonic contribution, has been experimentally confirmed with a 3σ significance.

F. Electroweak effect

The contribution of Z^0 exchanges (electroweak effect) can be made visible by comparing the measurement $(dR^{\mathrm{EB}}/d\Omega)$ with the QED prediction, the sum of the first three terms in Eq. (20). The ratio between them is plotted in Fig. 10. The solid curve shows the prediction from the standard improved-Born approximation, the sum of all ten terms in Eq. (20). The electroweak effect is obvious.

The importance of model-independent approaches was recently emphasized in experimental verification of the standard theory. The S-matrix method [38] has been proposed as one of the most general ways to realize this approach. In this method, the coupling constants are given independently for each helicity combination of the initial and final states, in terms of complex residua of the propagators. Among the many parameters to be experimentally determined in this approach, those concerning the Z^0 propagator and the Z^0 coupling constants, including the relative phases between them, can be precisely determined by experiments on the Z^0 resonance. We are less sensitive to them. What we are more sensitive to is the overall phase relation between the Z^0 couplings and the QED (photon) coupling.

At TRISTAN energies, the Z^0 exchanges are expected to contribute to Bhabha scattering dominantly via interferences with photon exchanges. The oscillatory structure of the standard theory prediction in Fig. 10 reflects this expectation. The $Z_s\gamma_t$ interference, the interference between the s-channel Z^0 exchange and the t-channel photon exchange, induces the enhancement at smaller scattering angles, while the $Z_s\gamma_s$ interference dominantly contributes to the enhancement in the backward region. The $Z_t\gamma_t$ interference shows a destructive effect, and dominates the negative correction near $\cos\theta=0$. If there were a sizable phase difference between the Z^0 couplings and the photon coupling, it would alter these interferences and affect the angular distribution.

The overall phase difference can be introduced by the following replacement:

$$\alpha_Z(q^2)\rightarrow e^{i\phi_Z}\alpha_Z, \quad \alpha_Z=\frac{G_F M_Z^2}{8\sqrt{2}\pi}. \tag{24}$$

Here, we assume $\rho(q^2)=1$. This modification appears in the improved-Born approximation, Eq. (20), as the following replacements:

$$(s-M_Z^2)\alpha_Z(s)\rightarrow\alpha_Z\left\{(s-M_Z^2)\cos\phi_Z+\frac{s\Gamma_Z}{M_Z}\sin\phi_Z\right\},$$

$$\alpha_Z(t)\rightarrow\alpha_Z\cos\phi_Z. \tag{25}$$

Since $s\Gamma_Z/M_Z$ is far smaller than $|s-M_Z^2|$ at our energy, the introduced phase difference predominantly acts to suppress the interference effects with the common factor of $\cos\phi_Z$. Fitting the modified improved-Born approximation to the experimental result, we obtained limits on the phase difference of

$$-0.24<\phi_Z/\pi<0.25 \tag{26}$$

at the 90% confidence level (C.L.).

G. Contact interaction

The consistency between the measurement and the standard theory can also be evaluated by considering new interactions. We examined the contact interaction hypothesis [39], because it has been studied by many experiments [40,41] and many of possible new interactions can be effectively described in terms of a contact interaction.

The cross section formula and terminology can be found in other reports [40]. A fit to the experimental result was carried out by assuming

$$\frac{dR^{\mathrm{EB}}/d\Omega}{dR^{\mathrm{EB}}_{\mathrm{EW}}/d\Omega}\cong\frac{dR^0/d\Omega}{dR^0_{\mathrm{EW}}/d\Omega}, \tag{27}$$

where 0 denotes a quantity evaluated from tree-level cross sections, i.e., $dR^0/d\Omega=d\sigma^0/d\Omega/\sigma^0_{\mathrm{EC}}$, and EW stands for the prediction from the standard electroweak theory. Obtained best-fit values of the contact interaction parameter,

$$\varepsilon=\pm\frac{1}{(\Lambda^{\pm})^2}, \tag{28}$$

are shown in Table VI for typical combinations of the coupling. The results for the LL and RR couplings are nearly the same, since their effects are almost identical at our energy. A summary of the results from experiments at PEP and PETRA [40] and a result from LEP [41] are listed as well. The present result shows the best sensitivity (the smallest error) among them.

TABLE VI. Best fit of the contact interaction parameter (ε). The results from previous measurements [38,39] are also listed.

	ε (TeV^{-2})				
	LL	*RR*	*AA*	*VV*	*LR*
This expt.	0.11±0.13	0.11±0.14	0.012±0.047	0.013±0.026	0.010±0.037
PEP and PETRA	0.23±0.21	0.22±0.21	−0.087±0.049	0.085±0.037	0.102±0.046
ALEPH	0.12±0.15	0.12±0.17	0.005±0.072	0.046±0.050	0.13±0.18

There has been a discussion about the definition of the lower limits on the contact interaction scale ($\Lambda^{\pm}$) [40,41]. The definition adopted by most of the experiments at the SLAC e^+e^- storage ring PEP and DESY e^+e^- collider PETRA [see Eqs. (22) and (23) in Ref. [40]] has an undesirable property; the extraction of the limit on either Λ^+ or Λ^- fails with a finite probability (10% for the 95% C.L. limits), even if there is no contact interaction. This is crucial since we cannot make any reasonable interpretation of such failed results. The ALEPH group introduced an alternative in order to cover this defect [41], though it looks rather artificial.

Instead, we adopted a simple definition which arises from the recommendation from PDG concerning the definition of the confidence level under the existence of physical boundaries [31]. We defined the upper limits of ε at the 95% C.L., ε^+ and ε^-, as

$$\frac{\int_0^{\varepsilon^{\pm}} G(\pm\varepsilon;\overline{\varepsilon},\sigma_\varepsilon)d\varepsilon}{\int_0^{\infty} G(\pm\varepsilon;\overline{\varepsilon},\sigma_\varepsilon)d\varepsilon}=0.95, \tag{29}$$

where $G(\varepsilon;\overline{\varepsilon},\sigma_\varepsilon)$ is a Gaussian probability function with a mean of $\overline{\varepsilon}$ and a standard deviation of σ_ε. The parameters $\overline{\varepsilon}$ and σ_ε are the best fit of ε and its error, respectively, presented in Table VI. The Gaussian probability was adopted because the χ^2 shows a nearly ideal parabolic behavior when we choose ε as a fitting parameter.

The lower limits on $\Lambda^{\pm}$ were then determined as $1/\sqrt{\varepsilon^{\pm}}$. The obtained limits are listed in Table VII, together with reevaluated limits for the PEP and PETRA, and LEP results. We have obtained limits of 1.7–4.8 TeV, depending on the coupling. The limits are comparable with or better than those from the previous experiments.

We tried another approach within the context of the contact interaction, where ε_{LL}, ε_{RR}, and ε_{LR} $(=\varepsilon_{RL})$ were allowed to vary simultaneously. Models of heavy particle exchanges can be expressed in many cases in terms of the contact interaction, when the particle mass is sufficiently larger than the c.m. energy. This is an analogy to the Fermi coupling of the weak interaction at low energies. In such cases, the coupling is not necessarily one of the typical ones that we have examined in the above. The result of the simultaneous fit can be converted to constraints on such models with simple calculations, without retrying any fit.

In this analysis, in order to make the result simpler, the error from the end-cap measurement (0.7%) was added to the error matrix as a normalization error; i.e., $(0.007)^2x_ix_j$ was added. Accordingly, the normalization factor was fixed to the unity and the corresponding constraint term was omitted from the χ^2 definition. The obtained best fit and the error correlation are presented in Table VIII. Here, $\varepsilon_1=\varepsilon_{LL}+\varepsilon_{RR}$, $\varepsilon_2=\varepsilon_{LL}-\varepsilon_{RR}$, and $\varepsilon_3=\varepsilon_{LR}$ are chosen as fitting parameters, because ε_{LL} and ε_{RR} have a very strong negative correlation. The coupling strength of new interactions allowed by the result is smaller by a factor of about 20 than the corresponding Fermi-coupling strength, $\sqrt{2}G_F/\pi=5.3$ TeV^{-2}, unless $\varepsilon_{LL}+\varepsilon_{RR}$ and ε_{LR} are simultaneously small.

If a model includes an unknown parameter ε and the interaction can be interpreted as $\varepsilon_m=\xi_m\varepsilon$ $(m=1,2,3)$, the optimum value $(\overline{\varepsilon})$ and error (σ_ε) of ε are given by the fitting result as

$$\overline{\varepsilon}=\frac{\sum_{m,n} C^{-1}_{mn}\xi_m\overline{\varepsilon_n}}{\sum_{m,n} C^{-1}_{mn}\xi_m\xi_n} \quad \text{and} \quad \frac{1}{\sigma_\varepsilon^2}=\sum_{m,n} C^{-1}_{mn}\xi_m\xi_n\,. \tag{30}$$

The error matrix is defined as $C_{mn}=\rho_{mn}\sigma_{\varepsilon_m}\sigma_{\varepsilon_n}$. The parameters $\overline{\varepsilon_m}$, σ_{ε_m}, and ρ_{mn} are the optimum value and the error of ε_m and the error correlation, respectively, presented in Table VIII. The results in Table VI, where $\varepsilon_{ij}=\eta_{ij}\varepsilon$ $(\eta_{ij}=\pm1$ or 0), are reproduced by Eq. (30) with reasonable tolerances. The results are not exactly the same because of the different treatment of the end-cap error.

TABLE VII. Obtained lower limits of the contact interaction scale Λ at the 95% C.L. The limits have been evaluated according to the new definition described in the text. Reevaluated limits for the results from previous measurements are shown for comparison.

	Lower limits of Λ (TeV)									
	LL		*RR*		*AA*		*VV*		*LR*	
	+	−	+	−	+	−	+	−	+	−
This expt.	1.7	2.3	1.7	2.2	3.2	3.4	4.1	4.8	3.6	3.9
PEP and PETRA	1.3	1.9	1.3	1.9	4.3	2.4	2.6	5.3	2.4	4.7
ALEPH	1.6	2.1	1.5	2.0	2.6	2.9	2.7	3.7	1.5	1.9

TABLE VIII. Best fit of the contact interaction parameters, $\varepsilon_1=\varepsilon_{LL}+\varepsilon_{RR}$, $\varepsilon_2=\varepsilon_{LL}-\varepsilon_{RR}$, and $\varepsilon_3=\varepsilon_{LR}$, obtained from the simultaneous fit. The error correlation is shown as well.

	Best fit (TeV^{-2})	Correlation	
		ε_1	ε_2
ε_1	0.14 ± 0.17		
ε_2	0.13 ± 1.93	0.007	
ε_3	-0.016 ± 0.045	-0.63	0.064

As an example of specific models, we examined the hypothesis of extra-Z bosons from the E_6 unification model [42]. Their contribution of Bhabha scattering can be approximated by a contact interaction, defined as

$$\varepsilon_{ij} = -\alpha g^e_{2i}(\beta) g^e_{2j}(\beta) \frac{1}{M^2_{Z_2}} \quad (i,j=L,R), \tag{31}$$

if the mass of the extra-Z boson (M_{Z_2}) is sufficiently large. The coupling constants $g^e_{2i}(\beta)$ are determined if the model parameter β is fixed. Thus, Eq. (30) can be applied if we take $\varepsilon = M^{-2}_{Z_2}$ and the coefficients as

$$\xi_1 = -\alpha[g^e_{2L}(\beta)^2 + g^e_{2R}(\beta)^2],$$

$$\xi_2 = -\alpha[g^e_{2L}(\beta)^2 - g^e_{2R}(\beta)^2],$$

$$\xi_3 = -\alpha g^e_{2L}(\beta) g^e_{2R}(\beta). \tag{32}$$

For the Z_χ model, where $\beta=\pi/2$, we obtain a constraint of $\varepsilon=-9\pm17$ TeV^{-2}, if the mixing with the standard-model Z^0 is negligible. The constraint can be converted to a lower mass limit of 190 GeV/c^2 by using the definition of ε^+ in Eq. (29). The mass limits are less significant for other variations of the model, because of smaller couplings to the electron.

H. Neutral scalar exchange

In our previous report [13], we examined possible effects of heavy neutral scalar particle exchanges, using the integrated cross section of Bhabha scattering at large angles measured at various c.m. energies. The angular distribution gives supplementary information on this subject. A fit was tried by using the cross section formula in Ref. [43]. The obtained upper limit on the partial decay width Γ_{ee} of the scalar particles at the 95% C.L. is drawn in Fig. 11, together with the limits from the previous study. The new limit is better than the previous ones in a large-mass region, >65 GeV/c^2, where the dependence on the total decay width is indistinguishable. The limit is about 25 MeV around the Z^0 mass.

VI. CONCLUSION

Bhabha scattering was measured at a c.m. energy of 57.77 GeV using the VENUS detector at TRISTAN. The precision of 0.5% has been achieved in the central region, $|\cos\theta| \leq 0.743$, and 0.7% in the forward region, $0.822 \leq \cos\theta \leq 0.968$. A model-independent scattering angle distribution, $R_i = \sigma_i/\sigma_{\mathrm{EC}}$, was extracted from the measurement. Error correlation between angular bins was treated in the form of an error (covariance) matrix and implemented in all quantitative discussions. The obtained scattering angle distribution was found to be in good agreement with the prediction from the standard electroweak theory. No evidence for new physics nor discrepancy with the standard theory has been found.

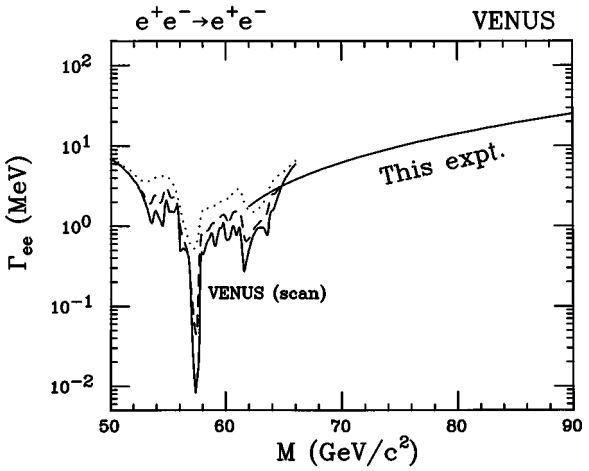

FIG. 11. Upper limit at the 95% C.L. on the partial decay width Γ_{ee} of neutral scalar particles. The limit is shown as a function of the assumed scalar particle mass. The limits obtained in our previous study [12] are shown for three cases of the assumed total decay width: 0.5 GeV (solid), 1 GeV (dashed), and 2 GeV (dotted). The limit newly established by this experiment is insensitive to the total decay width.

Discussions concerning the underlying physics have been carried out by using an angular distribution defined under the effective-Born concept, $dR^{\mathrm{EB}}/d\Omega = [d\sigma^{\mathrm{EB}}/d\Omega]/\sigma^{\mathrm{EB}}_{\mathrm{EC}}$, where photon-radiation effects are unfolded. The q^2-running effect of the QED fine-structure constant α has been directly observed with the significance of three standard deviations. The phenomenological prediction concerning the hadronic contribution to the running has been confirmed with 2σ significance. An electroweak (Z^0 exchange) effect has been clearly observed. The agreement with the standard theory leads us to a limit on the possible phase difference between the photon and Z^0 couplings, as $-0.24 < \phi_Z/\pi < 0.25$ at the 90% C.L.

The contact interaction hypothesis has been examined as another measure of the consistency between the measurement and the standard theory. A simple and rational definition for the limits on the contact interaction scale has been introduced. The obtained lower limits at the 95% C.L. are from 1.7 to 4.8 TeV, depending on the combination of the helicity states of the coupling electrons. They are comparable with or better than the limits from previous experiments.

In addition, another approach to new physics has been tried in the context of the contact interaction, where interactions are assumed to be relevant to arbitrary combination of the helicity states of the electron. The coupling strength allowed by the fitting result is smaller by a factor of about 20 than the Fermi coupling of the weak interaction, unless the coupling is quite exotic. The result can be converted to constraints on specific models with a simple calculation. A lower mass limit on an extra Z boson has been extracted as an example.

The effect of heavy neutral scalar-particle exchanges has been examined as a supplement to our previous study. A new limit has been established in a large-mass region (>65 GeV/c^2), which corresponds to a 95% C.L. limit of $\Gamma_{ee}<25$ MeV around the Z^0 mass.

ACKNOWLEDGMENTS

We wish to thank the TRISTAN machine group for their patient efforts regarding the accelerator operation that continued for many years. We gratefully acknowledge the outstanding contributions of the technical staff at KEK and the collaborating institutes who participated in the construction and operation of the VENUS detector. The data acquisition and analyses were made possible with continuous support by people from the on-line group and the computer center of KEK. We thank K. Hagiwara for a useful discussion. We also thank W. Beenakker for advice and discussions concerning the use of ALIBABA.

[1] VENUS Collaboration, K. Abe *et al.*, J. Phys. Soc. Jpn. **56**, 3767 (1987).

[2] TOPAZ Collaboration, I. Adachi *et al.*, Phys. Lett. B **200**, 391 (1988); AMY Collaboration, S. K. Kim *et al.*, *ibid.* **223**, 476 (1989).

[3] CELLO Collaboration, H. J. Behrend *et al.*, Z. Phys. C **51**, 143 (1991); JADE Collaboration, W. Bartel *et al.*, *ibid.* **19**, 197 (1983); **30**, 371 (1986); PLUTO Collaboration, Ch. Berger *et al.*, *ibid.* **27**, 341 (1985); HRS Collaboration, M. Derrick *et al.*, Phys. Lett. **116B**, 463 (1986); Phys. Rev. D **34**, 3286 (1986); MAC Collaboration, E. Fernandez *et al.*, *ibid.* **35**, 10 (1987); TASSO Collaboration, W. Braunschweig *et al.*, Z. Phys. C **37**, 171 (1988).

[4] P. B. Renton, in *17th International Symposium on Lepton-Photon Interactions*, edited by Z.-P. Zheng and H.-S. Chen (World Scientific, Singapore, 1996), p. 35.

[5] S. Weinberg, Phys. Rev. Lett. **19**, 1264 (1967); A. Salam, in *Elementary Particle Theory: Relativistic Groups and Analyticity (Nobel Symposium No. 8)*, edited by N. Svartholm (Almqvist and Wiksells, Stockholm, 1968), p. 267.

[6] F. A. Berends, K. J. F. Gaemers, and R. Gastmans, Nucl. Phys. **B68**, 541 (1974).

[7] K. Tobimatsu and Y. Shimizu Prog. Theor. Phys. **74**, 567 (1985); **76**, 334 (1986); **75**, 905 (1986); S. Kuroda *et al.*, Comput. Phys. Commun. **48**, 335 (1988).

[8] M. Böhm, A. Denner, and W. Hollik, Nucl. Phys. **B304**, 687 (1988); F. A. Berends, R. Kleiss, and W. Hollik, *ibid.* **B304**, 712 (1988).

[9] W. Beenakker, F. A. Berends, and S. C. van der Marck, Nucl. Phys. **B349**, 323 (1991).

[10] G. Montagna *et al.*, Nucl. Phys. **B401**, 3 (1993); Comput. Phys. Commun. **76**, 328 (1993); H. Anlauf *et al.*, *ibid.* **79**, 466 (1994); M. Caffo, H. Czyz, and E. Remiddi, Phys. Lett. B **327**, 369 (1994); J. H. Field, *ibid.* **323**, 432 (1994); J. Fujimoto, Y. Shimizu, and T. Munehisa, Prog. Theor. Phys. **91**, 333 (1994).

[11] TRISTAN Project Group, *TRISTAN Electron-positron Colliding Beam Project*, KEK 86-14 (1987).

[12] K. Nakajima (unpublished).

[13] VENUS Collaboration, K. Abe *et al.*, Phys. Lett. B **302**, 119 (1993).

[14] H. Fukuma, in *Proceedings the Workshop on TRISTAN Physics at High Luminosities*, 1992, edited by M. Yamauchi, KEK Proceedings 93-2 (1993), p. 296.

[15] VENUS Collaboration, K. Abe *et al.*, J. Phys. Soc. Jpn. **56**, 3763 (1987).

[16] Y. Yamada *et al.*, Nucl. Instrum. Methods Phys. Res. A **330**, 64 (1993).

[17] M. Sakuda *et al.*, Nucl. Instrum. Methods Phys. Res. A **311**, 57 (1992).

[18] R. Arai *et al.*, Nucl. Instrum. Methods Phys. Res. A **254**, 317 (1987).

[19] R. Arai *et al.*, Nucl. Instrum. Methods Phys. Res. A **217**, 181 (1983); S. Odaka, KEK Report No. 88-5, 1988 (unpublished).

[20] Y. Hemmi *et al.*, Jpn. J. Appl. Phys. **26**, 982 (1987).

[21] K. Ogawa *et al.*, Nucl. Instrum. Methods Phys. Res. A **243**, 58 (1986); T. Sumiyoshi *et al.*, *ibid.* **271**, 432 (1988).

[22] Y. Fukushima *et al.*, IEEE Trans. Nucl. Sci. **NS-36**, 670 (1989).

[23] F. Takasaki *et al.*, Nucl. Instrum. Methods Phys. Res. A **322**, 211 (1992).

[24] Y. Asano *et al.*, Nucl. Instrum. Methods Phys. Res. A **254**, 35 (1987); Y. Asano *et al.*, *ibid.* **259**, 430 (1987).

[25] T. Ohsugi *et al.*, Nucl. Instrum. Methods Phys. Res. A **269**, 522 (1988).

[26] Y. Arai and S. Uehara, Nucl. Instrum. Methods Phys. Res. A **301**, 497 (1991).

[27] M. Derrick *et al.*, Phys. Rev. D **34**, 3286 (1986). The bremsstrahlung formula presented in this article was found to be practically equivalent to a formula given in J. Nishimura, *Theory of Cascade Shower*, Handbuch der Physik Vol. XLVI/2, Cosmic Ray II (Springer-Verlag, Berlin, 1967), p. 1.

[28] K. Tobimatsu and Y. Shimizu, Comput. Phys. Commun. **55**, 337 (1989).

[29] M. Igarashi *et al.*, Nucl. Phys. **B263**, 347 (1986).

[30] T. Sjöstrand and M. Bengtsson, Comput. Phys. Commun. **46**, 43 (1987); **39**, 347 (1986); M. Bengtsson and T. Sjöstrand, Phys. Lett. B **185**, 435 (1987).

[31] Particle Data Group, L. Montanet *et al.*, Phys. Rev. D **50**, 1173 (1994).

[32] F. A. Berends, P. H. Daverveldt, and R. Kleiss, Comput. Phys. Commun. **40**, 285 (1986).

[33] J. Fujimoto and M. Igarashi, Prog. Theor. Phys. **74**, 791 (1985); J. Fujimoto, M. Igarashi, and Y. Shimizu, *ibid.* **77**, 118 (1987).

[34] The calculation with ALIBABA was not straightforward, owing to constraints on the angular acceptance required in ALIBABA. Certain manipulations of the results, subtractions and additions, were indispensable. In addition, in order to preserve a sufficient numerical accuracy, the number of trials was increased in the Monte Carlo integration for the evaluation of nonlogarithmic terms.

[35] M. Consoli and W. Hollik, in *Z Physics at LEP 1*, edited by G. Altarelli *et al.*, CERN 89-08 (1989), Vol. 1, p. 7; M. Caffo and E. Remmidi, *ibid.*, p. 171; D. Bardin, W. Hollik, and T. Rie-

mann, Z. Phys. C **49**, 485 (1991); M. Martinez and R. Miquel, *ibid.* **53**, 115 (1992); **58**, 15 (1993).
[36] H. Burkhardt, F. Jegerlehner, G. Penso, and C. Verzegnassi, Z. Phys. C **43**, 497 (1989).
[37] TOPAZ Collaboration, K. Miyabayashi *et al.*, Phys. Lett. B **347**, 171 (1995).
[38] A. Borrelli, M. Consoli, L. Maiani, and R. Sisto, Nucl. Phys. **B333**, 357 (1990); L. Leike, T. Riemann, and J. Rose, Phys. Lett. B **273**, 513 (1991); G. Isidori, *ibid.* **314**, 139 (1993).
[39] E. J. Eichten, K. D. Lane, and M. E. Peskin, Phys. Rev. Lett. **50**, 811 (1983).
[40] H. Kroha, Phys. Rev. D **46**, 58 (1992), and references therein.
[41] ALEPH Collaboration, D. Buskulic *et al.*, Z. Phys. C **59**, 215 (1993).
[42] K. Hagiwara *et al.*, Phys. Rev. D **41**, 815 (1990); VENUS Collaboration, K. Abe *et al.*, Phys. Lett. B **246**, 297 (1990).
[43] W. Hollik, F. Schrempp, and B. Schrempp, Phys. Lett. **140B**, 424 (1984).